nature protocols

PROTOCOL

https://doi.org/10.1038/s41596-023-00829-4

Check for updates

Spatial- and Fourier-domain ptychography for high-throughput bio-imaging

Shaowei Jiang[1,5], Pengming Song[1,5], Tianbo Wang[1,5], Liming Yang[1], Ruihai Wang[1], Chengfei Guo[1,2], Bin Feng[1], Andrew Maiden[3,4] and Guoan Zheng[1]✉

First envisioned for determining crystalline structures, ptychography has become a useful imaging tool for microscopists. However, ptychography remains underused by biomedical researchers due to its limited resolution and throughput in the visible light regime. Recent developments of spatial- and Fourier-domain ptychography have successfully addressed these issues and now offer the potential for high-resolution, high-throughput optical imaging with minimal hardware modifications to existing microscopy setups, often providing an excellent trade-off between resolution and field of view inherent to conventional imaging systems, giving biomedical researchers the best of both worlds. Here, we provide extensive information to enable the implementation of ptychography by biomedical researchers in the visible light regime. We first discuss the intrinsic connections between spatial-domain coded ptychography and Fourier ptychography. A step-by-step guide then provides the user instructions for developing both systems with practical examples. In the spatial-domain implementation, we explain how a large-scale, high-performance blood-cell lens can be made at negligible expense. In the Fourier-domain implementation, we explain how adding a low-cost light source to a regular microscope can improve the resolution beyond the limit of the objective lens. The turnkey operation of these setups is suitable for use by professional research laboratories, as well as citizen scientists. Users with basic experience in optics and programming can build the setups within a week. The do-it-yourself nature of the setups also allows these procedures to be implemented in laboratory courses related to Fourier optics, biomedical instrumentation, digital image processing, robotics and capstone projects.

Introduction

Phase information characterizes how much a light wave is delayed by propagation through a sample. However, light detectors can only measure intensity variations of the light wave, leading to the loss of the associated phase information, referred to as the ‘phase problem’. This term originates from the field of crystallography[1], where the phase problem needs to be solved to determine the structure of a crystal from diffraction measurements. Ptychography was originally developed in 1969 to solve the phase problem of electron crystallography[2]. By measuring diffraction data as a narrow coherent probe beam translated across a crystalline specimen, it aimed to extract the phase of the crystal’s Bragg peaks—the interference maxima caused by crystal lattice scattering—and thereby recover a real-space image of the crystal structure. The name ‘ptychography’ (pronounced tie-KOH-gra-fee) was derived from the Greek ptycho, meaning to fold in English and convolution in German[3]. It was chosen to highlight the spatial-domain interaction between the probe beam and the crystalline specimen, which can be modeled by a Fourier-domain convolution between the Bragg peaks and the probe’s Fourier spectrum. Although the experimental and computational implementations of ptychography have changed considerably since its inception, convolution in reciprocal space remains a key aspect of the technology and the name remains appropriate today.

Since its conceptualization in 1969, it has taken several developments to make ptychography a practical and appealing imaging technique. One notable advance was the adoption of an iterative phase retrieval framework for image reconstruction, which brought the technique to its modern form[4]. The experimental procedure remains the same: the object under testing is translated through a spatially confined probe beam and the corresponding diffraction patterns are recorded in reciprocal space (Fig. 1a). Unlike the original concept, however, which used an analytic inversion method that

---

[1]Department of Biomedical Engineering, University of Connecticut, Storrs, USA. [2]Hangzhou Institute of Technology, Xidian University, Hangzhou, China. [3]Department of Electronic and Electrical Engineering, University of Sheffield, Sheffield, UK. [4]Diamond Light Source, Harwell Science and Innovation Campus, Chilton, UK. [5]These authors contributed equally: Shaowei Jiang, Pengming Song, Tianbo Wang. ✉e-mail: guoan.zheng@uconn.edu

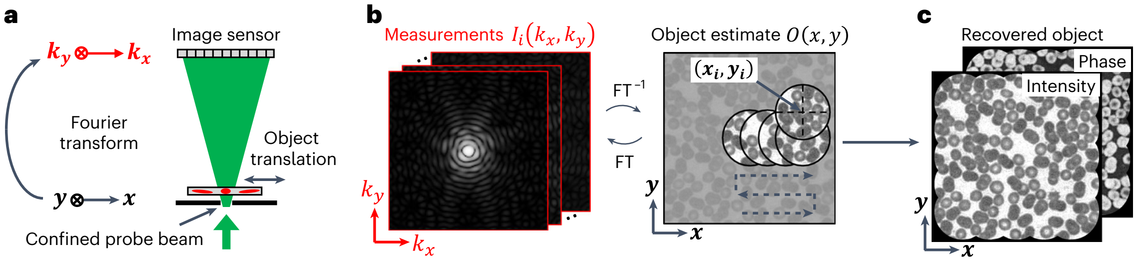

Fig. 1 | The modern form of ptychography. **a**, The complex-valued object $O(x,y)$ is translated through a spatially confined probe beam $P(x,y)$. The product between the object profile and the probe beam propagates to the far-field via a Fourier transform. The diffraction measurement can be expressed as $I_i(k_x, k_y) = |\mathrm{FT}\{O(x - x_i, y - y_i) \cdot P(x, y)\}|^2$, where ($k_x$,$k_y$) are the coordinates of the Fourier plane, (x_i, y_i) is the *i*th translated position of the object and FT denotes the Fourier transform. The resulting dataset I_i (i = 1,2,3...) is a collection of diffraction measurements for all translated positions of the object. **b**, The reconstruction process iteratively imposes two constraints to recover the object profile. The first constraint imposes consistency in the overlapping illumination areas on the object surface and is implemented by updating the object estimate in real space. The second constraint is the Fourier magnitude constraint imposed in reciprocal space. It is implemented by replacing the modulus of the estimated diffraction pattern with the square-root of the corresponding measured intensity whilst keeping the phase unchanged. **c**, The iterative process converges to an object image with both intensity and phase properties.

required an impractically large number of measurements, modern ptychography iteratively recovers the object from a substantially smaller dataset by imposing two sets of constraints. In real space, the translation of the object through the probe beam results in a patchwork of overlapping illumination areas on the object surface, and the reconstructed object image must be consistent in these overlapping areas. In reciprocal space, the diffraction measurements serve as constraints on the reconstructed object image, whose Fourier transform must match the measured diffraction data for each position of the probe beam. The iterative reconstruction process of ptychography in Fig. 1b,c essentially looks for an object estimate that satisfies both constraints. As shown in the right panel of Fig. 1b, the overlapping areas of illumination during adjacent measurements is the key innovation offered by ptychography over other phase retrieval methods, since it both avoids ambiguities in the solution and accelerates the convergence speed of the phase retrieval process.

With the help of the iterative phase retrieval framework, ptychography has since evolved into an enabling microscopy technique where image-forming optics are replaced by computational reconstructions. Over the past decades, ptychography has attracted considerable attention from different research communities[3,5–7]. For coherent X-ray imaging, it has become an indispensable imaging tool at most synchrotrons and national laboratories worldwide[8]. For electron microscopy, recent work has pushed imaging resolution to record-breaking deep subangstrom levels[9]. For visible light imaging, new developments in spatial- and Fourier-domain ptychography[10–14] has offered unique solutions for high-resolution, high-throughput optical imaging with minimal hardware modifications.

To facilitate the uptake of ptychography by biomedical researchers in different fields, here we provide a comprehensive protocol detailing the implementation of both spatial-domain coded ptychography (CP) and Fourier-domain ptychography (FP) in the visible light regime[10–14]. We present alternative methods, examine the advantages and limitations of different ptychographic implementations, and identify the critical steps and pitfalls that may occur during experiments. Users with basic experience in optics and programming can complete the setups and perform ptychographic reconstructions in ~1 week. The do-it-yourself nature of the setups also allows this protocol to be implemented in laboratory courses related to Fourier optics, biomedical instrumentation, digital image processing, robotics and capstone design projects.

Development of the protocol

Built upon the modern form of ptychography, FP and CP are two variants that are designed to achieve high-resolution, high-throughput imaging with visible light. The FP approach was developed in 2013 to improve the resolution of a regular lens-based microscope beyond the diffraction limit set by the objective lens[10]. A typical FP setup consists of a programmable light-emitting diode (LED) array and a regular microscope with a low numerical aperture (NA) objective lens. The system configuration in Fig. 2 defines three planes for the FP setup: the specimen at the object plane (x,y), the pupil aperture at the Fourier plane (k_x,k_y) and the detector at the image plane (x,y). The objective lens performs a Fourier transform to convert the light waves from the object plane (x,y) to the aperture plane (k_x,k_y). The tube lens performs a second Fourier transform to convert the light waves from the

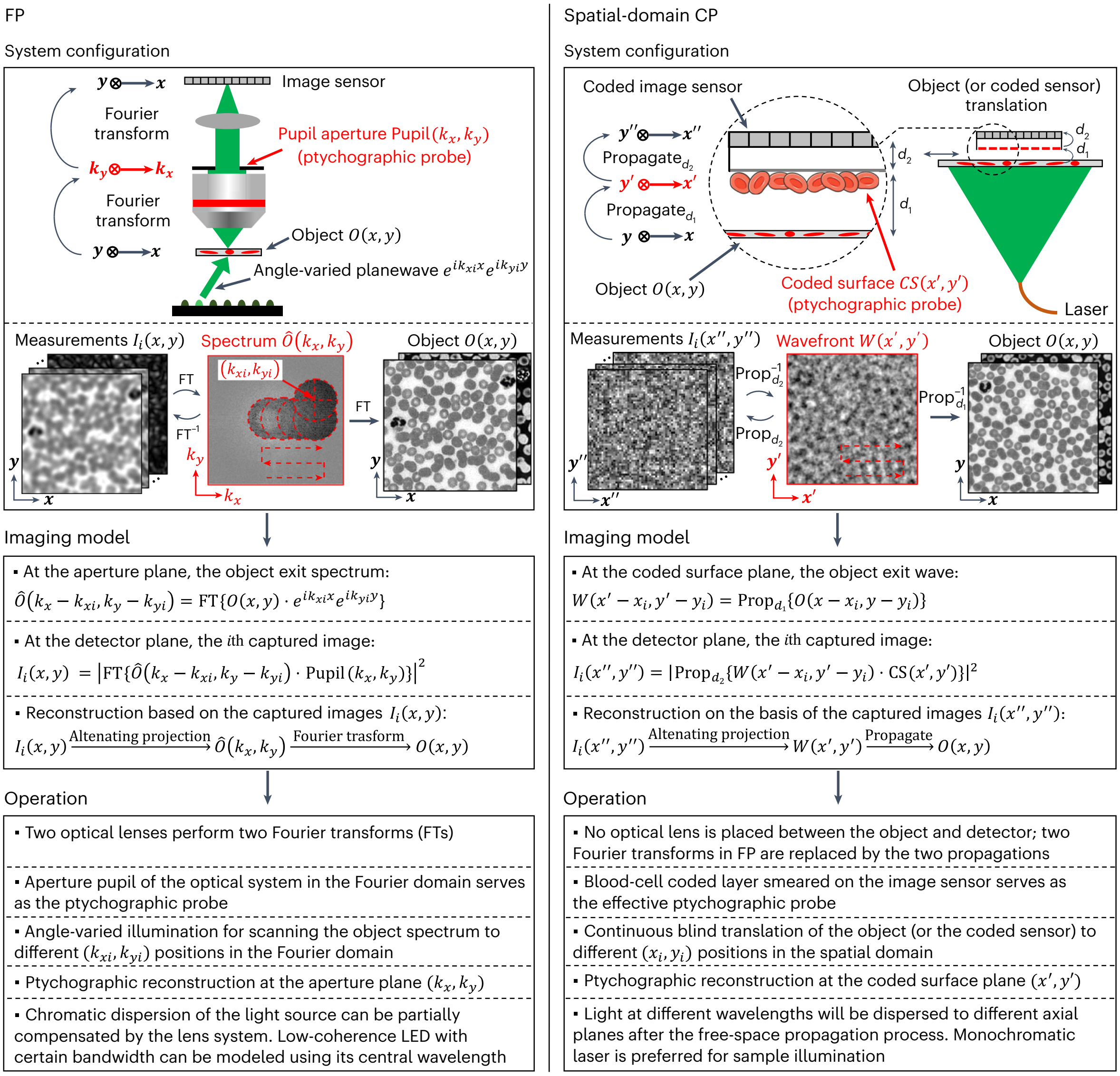

Imaging model

- At the aperture plane, the object exit spectrum:
$\hat{O}(k_x - k_{xi}, k_y - k_{yi}) = \mathrm{FT}\{O(x,y)\cdot e^{ik_{xi}x}e^{ik_{yi}y}\}$
- At the detector plane, the *i*th captured image:
$I_i(x,y) = \left|\mathrm{FT}\{\hat{O}(k_x - k_{xi}, k_y - k_{yi})\cdot \mathrm{Pupil}(k_x,k_y)\}\right|^2$
- Reconstruction based on the captured images $I_i(x,y)$:
$I_i(x,y) \xrightarrow{\text{Altenating projection}} \hat{O}(k_x,k_y) \xrightarrow{\text{Fourier trasform}} O(x,y)$

Operation

- Two optical lenses perform two Fourier transforms (FTs)
- Aperture pupil of the optical system in the Fourier domain serves as the ptychographic probe
- Angle-varied illumination for scanning the object spectrum to different (k_{xi}, k_{yi}) positions in the Fourier domain
- Ptychographic reconstruction at the aperture plane (k_x, k_y)
- Chromatic dispersion of the light source can be partially compensated by the lens system. Low-coherence LED with certain bandwidth can be modeled using its central wavelength

Imaging model

- At the coded surface plane, the object exit wave:
$W(x' - x_i, y' - y_i) = \mathrm{Prop}_{d_1}\{O(x - x_i, y - y_i)\}$
- At the detector plane, the *i*th captured image:
$I_i(x'',y'') = |\mathrm{Prop}_{d_2}\{W(x' - x_i, y' - y_i)\cdot \mathrm{CS}(x',y')\}|^2$
- Reconstruction on the basis of the captured images $I_i(x'',y'')$:
$I_i(x'',y'') \xrightarrow{\text{Altenating projection}} W(x',y') \xrightarrow{\text{Propagate}} O(x,y)$

Operation

- No optical lens is placed between the object and detector; two Fourier transforms in FP are replaced by the two propagations
- Blood-cell coded layer smeared on the image sensor serves as the effective ptychographic probe
- Continuous blind translation of the object (or the coded sensor) to different (x_i, y_i) positions in the spatial domain
- Ptychographic reconstruction at the coded surface plane (x', y')
- Light at different wavelengths will be dispersed to different axial planes after the free-space propagation process. Monochromatic laser is preferred for sample illumination

Fig. 2 | Spatial-domain CP and FP. Left: in the Fourier-domain implementation, a programmable LED array is used to illuminate the object with angle-varied plane waves. The captured images are used to recover the object spectrum in the Fourier domain. The recovered spectrum is then transformed back to the spatial domain to obtain a complex-valued object image. Right: in the spatial-domain implementation, a coded surface on the image sensor (e.g., a blood-cell layer) is used to modulate the diffracted light waves from the object. By translating the object (or the coded sensor) to different lateral positions, the corresponding captured images are used to recover the object's exit wavefront at the coded surface plane. This wavefront is then propagated to the object plane to obtain a high-resolution complex-valued object image.

aperture plane (k_x, k_y) to the image plane (x,y). In this imaging model, the pupil aperture in the Fourier plane effectively serves as a low-pass filter for the measurement in the image plane.

In the operation of FP, the LED array illuminates the object with plane waves at different incident angles and the system records the corresponding low-resolution intensity images $I_i(x,y)$ $(i = 1,2,\ldots)$. Each measurement corresponds to the information from a circular aperture region in Fourier space (see the 'Spectrum $\hat{O}(k_x, k_y)$' image in Fig. 2). The size of the aperture is determined by the NA of the objective whilst its offset from the origin is determined by the illumination wavevector (k_{xi}, k_{yi}) of the *i*th LED element. Following the iterative phase retrieval process, we can synthesize the measurements in the Fourier domain and recover the object spectrum $\hat{O}(k_x, k_y)$. The high-resolution object image $O(x,y)$ can then be obtained by transforming the synthesized spectrum back to the spatial domain (see the 'Imaging model' section in Fig. 2). The resolution of this recovered image is no longer limited by the employed objective lens. Instead, it is determined by the maximum incident angle of the LED array: the larger the maximum incident angle, the better the resolution. On the other hand, this image retains the original large field of view of the low-NA objective lens. Since its first demonstration, FP has evolved from a simple microscope tool to a general technique for different research communities[15–18]. For example, the FP concept has been integrated with diffraction tomography for high-resolution 3D microscopy imaging[19,20]. It has also been adopted in long-range synthetic aperture remote sensing[21–24] and implemented with coherent X-ray for dose-efficient nanoscopy[25].

Unlike the lens-based FP system, spatial-domain CP was developed to perform high-resolution, high-throughput imaging without using any optical lenses. It takes a downstream modulation scheme for coded detection[26–28], where the information encoding process is performed at the detection path. Compared with FP, CP replaces the lens system with a simple blood-cell layer coated on the image sensor. The system configuration in Fig. 2 defines three planes for a typical CP setup: the specimen at the object plane (x,y), the blood-cell layer at the modulation plane (x',y'), and the detector at the image plane (x'', y''). The light waves propagate for a distance d_1 from the object plane (x,y) to the modulation plane (x',y'), and a distance d_2 from the modulation plane (x', y') to the image plane (x'', y''). The blood-cell layer redirects light diffracted at a large angle by the object to smaller angles that can be detected by the pixel array. Therefore, previously inaccessible high-resolution object details can now be acquired using the image sensor[11,13]. To this end, the blood-cell layer serves as a high-resolution bio-lens with a theoretically unlimited field of view. It can unlock an optical space with spatial extent (x,y) and spatial frequency content (k_x,k_y) that is inaccessible using conventional lens-based optics. We also note that a disorder-engineered surface can replace the blood-cell layer in a CP setup[11]. However, preparation of the disorder-engineered surface often requires specialized tools and chemicals. In contrast, smearing blood on the sensor's coverglass offers a simple yet effective solution for developing a CP setup. With proper cell fixation, the blood-cell layer can preserve its morphology for a relatively long period of time.

In the operation of CP, a laser is coupled to a single-mode fiber and used to illuminate the object under imaging. By translating the object (or the blood-coated sensor) to different lateral positions, the system records a set of intensity images $I_i(x'', y'')$ $(i = 1,2,\ldots)$. Following the iterative phase retrieval process, the complex object exit wavefront $W(x', y')$ at the modulation plane is recovered. This wavefront is then propagated to the object plane to obtain the high-resolution object profile $O(x,y)$.

The intrinsic connections between FP and CP are summarized in the 'Imaging model' and 'Operation' sections of Fig. 2. With FP, the object locates in real space, and the two optical lenses transform it to reciprocal space and then back to real space again. The pupil aperture serves as the effective ptychographic probe in the Fourier plane. With CP, the object locates in real space, and the two propagation operations transform it to the modulation plane and then to the image plane. The blood-coated layer in CP serves as the effective ptychographic probe in the modulation plane. We can see that the two Fourier transform operations in FP are replaced by two free-space propagation operations in CP. Both FP and CP illuminate the specimen using an extended beam that covers a large area for image acquisition. This is a key consideration for high-throughput microscopy imaging.

One distinction between FP and CP is the employed light source: low-coherence LEDs for FP and a laser for CP. This difference can be explained by the temporal coherence requirements of the systems. With FP, chromatic dispersion can be partially compensated by the lenses of the microscope: light with a small spectral bandwidth (~15 nm for LEDs) can be brought to the same image plane. With CP, on the other hand, light at different wavelengths will be dispersed to different axial planes after free-space propagation. Therefore, CP has a more stringent requirement on the temporal coherence of the light source and the monochromatic laser is a more appropriate choice. However, it is also possible to model the captured images from an LED source as coherent state mixtures[29,30] in a CP experiment[31].

Alternative methods

Drawing connections and distinctions between the two ptychographic implementations and other microscopy techniques helps to further clarify their advantages and working principles. In the following, we discuss four related techniques: (1) the traditional ptychography approach, (2) structured illumination microscopy (SIM), (3) common lensless microscopy techniques and (4) lens-based robotic microscopes.

The traditional ptychography approach uses a spatially confined probe beam for object illumination (Fig. 1a). Such a probe beam often varies between different experiments due to the sample alignment or light-source instability issues. For example, it is challenging to place different specimens in the exact same position of the confined probe beam. As a result, one often needs to jointly recover both the object and the probe beam for each experiment[32–34], a problem referred to as blind ptychography. Unlike the confined probe used in traditional ptychography, FP uses the pupil aperture and CP uses the blood-cell layer as the effective probe. These probes are hardcoded into the imaging systems and once characterized they remain unchanged for subsequent experiments. The pupil aperture in FP does vary at different spatial locations of the object's field of view[35,36] and characterizing these spatially varying pupil aberrations can require expert knowledge of aberration modes[36]. In contrast, CP has the advantage that it does not use any optical lenses in the setup and as a result, its ptychographic probe (the blood-cell layer) remains spatially invariant for different regions of the object.

SIM uses nonuniform intensity patterns (e.g., sinusoidal and random speckle patterns) to modulate high-frequency object information into the passband of the optical system[37]. In contrast, different plane waves are used for sample illumination in FP. The real-space product of the object and the plane wave corresponds to a shift of the object spectrum in the Fourier space. Therefore, the otherwise undetectable high-frequency object details can now be seen by the detector. Similarly, CP uses the blood-cell layer to redirect light waves with large diffraction angles into smaller angles for detection. As such, the blood-cell layer serves the role of a nonuniform illumination pattern similar to that used in SIM. We note that, however, the intensity-based nature of SIM allows it to be implemented for incoherent fluorescence microscopy. On the other hand, FP and CP are coherent imaging modalities and cannot be directly applied to incoherent imaging. When the same objective lens is used for both pattern projection and object detection in SIM, the resolution enhancement factor is limited to 2. The resolution enhancement factor of FP can well exceed 2 by using a low-NA lens for image acquisition. The highest synthetic NA demonstrated for FP is 1.9 in free space[38], close to the maximum possible synthetic NA of 2. The resolution of CP is determined by the largest diffraction angle that can be detected and this angle corresponds to an NA of 1 in free space, with the highest resolution currently achieved equivalent to an NA of ~0.8 (ref. [11]). We note that it is also possible to perform angle-varied illumination in CP to synthesize a maximum possible synthetic NA of 2.

Conventional multiheight lensless microscopy introduces different object-to-detector distances (or equivalently, different illumination wavelengths) to obtain multiple measurements for phase retrieval. The concept was first proposed in 1968 for electron microscopy[39] and has shown great potential for lensless imaging in the visible light regime[40–42]. However, it is challenging for this technique to recover the correct phase of the object. The reason can be explained by the concept of the phase transfer function, which characterizes the transfer of phase content at different spatial frequencies through an optical system[43]. For low-frequency content, the phase transfer function is close to 0 for multiheight measurements. Therefore, the low-frequency content is lost during the image acquisition process and cannot be restored from the subsequent phase retrieval process. A simple example helps to better illustrate this problem. In this thought experiment, an optical prism is placed on top of the image sensor and illuminated with a plane wave. The resulting multiheight measurements would be a constant value at each height and the phase delay introduced by the prism cannot be distinguished from free space. Thus, it is impossible to algorithmically restore the linear phase ramp from these measurements. The issue raised by this thought experiment also applies to other conventional lensless microscopy techniques, including the support-constraint approach[44,45], digital in-line holography[46], the transport-of-intensity approach[43] and blind ptychography with a unknown probe beam. With CP, on the other hand, the blood-cell layer can effectively convert the object phase information into distortions in the diffraction patterns. Thus, CP enables true quantitative phase recovery for all spatial frequency content with high sensitivity[11]. Also, the field of view of conventional lensless techniques is often limited to the area of the sensing surface, typically 20–40 mm^2. In contrast, the lateral translation operation of CP naturally expands the field of view beyond the sensor size. With these combined advantages, time-lapse monitoring of bacterial growth with a 120 mm^2 field of view, a 15 s per frame temporal resolution and a nanometer-range phase sensitivity has been demonstrated recently[14]. It should be noted that the concept of CP can be adopted for multiheight lensless imaging, although the resolution achieved is generally lower than that of CP due to the insufficient measurement diversity provided by the multiheight data[47].

Lens-based robotic microscopes have advanced notably in recent years, with a key milestone accomplished in 2017 when a whole-slide scanner was approved for primary diagnostic use in the United States[48]. However, such systems are costly and often have demanding requirements on mechanical stability. Images of microscope slides often fall out of focus due to the small depth of field of the employed high-NA objective lenses[49]. Similarly, in culture-based experiments, one often needs to constantly adjust the focus knob in a time-lapse experiment. Current autofocusing systems in robotic microscopes (e.g., the Nikon Perfect Focus) perform real-time tracking of a reference surface at the interface between the air and Petri dish. The user can then specify an offset distance related to the reference surface for image acquisition. However, the thickness of the dish substrate is not uniform, and the offset distance varies when the user scans different regions of the dish. Thus, it is challenging to perform large-scale monitoring of Petri dishes or multiwell plates over time. With both FP and CP, one can perform postmeasurement refocusing, which eliminates the need to maintain a precise distance between the sample and the imaging system. With CP, the recovered wavefront can be digitally propagated to any position along the optical axis postmeasurement. The translated x–y positions of the object can also be directly recovered from the CP measurements[50], allowing open-loop optical acquisition without requiring any feedback from the mechanical stage. To improve the imaging throughput, lens-based robotic microscopes scan the samples at high speed. The resultant motion blur needs to be addressed using pulsed illumination or time-delay-integration detection. In contrast, the scanning step size between adjacent CP measurements is at the micron level, therefore the sample can be in continuous motion without extra pulsed-illumination hardware. Lastly, it is challenging to perform parallel imaging using conventional robotic microscope systems. The scaling of complexity in array microscopy is an obstacle that prevents large-scale, high-throughput imaging for biomedical applications. For example, in drug screening, it is challenging to monitor cell culture growth in real time across all wells simultaneously. In contrast, parallel optical processing using both FP and CP has been demonstrated using multiple image sensors[11,51,52]. With FP, a parallel microscope system can simultaneously image all wells on a 96-well plate[51]. With CP, gigapixel high-resolution microscopic images with a 240 mm^2 effective field of view can be acquired in 15 s using an array of eight coded sensors[11].

Advantages and limitations

The competition between resolution and field of view is a long-standing problem in conventional microscopy systems. FP and CP can address this intrinsic trade-off, offering a unique solution for high-resolution, high-throughput optical imaging with minimal hardware modifications. The imaging acquisition speed can be orders of magnitude higher than conventional robotic microscopes at a small fraction of the cost[11]. Unlike holography, both FP and CP do not require a stable reference beam for interferometric measurement, enabling the use of partially coherent light sources such as LEDs for sample illumination. Additionally, they eliminate the isolated object requirement in conventional phase retrieval approaches[44,45], allowing contiguously connected samples to be imaged over an extended area. The lensless nature of CP further allows it to be implemented in the extreme ultraviolet and X-ray regimes, where high-resolution lenses are costly and challenging to make. Both FP and CP also produce a quantitative complex-valued image that reveals the absorption and phase-shift properties of the specimen. The capability for quantitative phase imaging enables high-contrast, label-free imaging of transparent biospecimens and is one motive for visible light and electron microscopy implementations. The richness of the datasets acquired by FP and CP further enables characterization of optical components in the experimental setup, such as measuring and correcting the effects of partial spatial and temporal coherence in light sources[53] and computationally compensating for optical aberrations in microscope systems[35,36,54]. In recent years, the unique benefits of FP and CP have led to various biomedical imaging applications, including high-throughput digital pathology[11,12,55–57], 2D and 3D quantitative phase imaging[19,20,54,58–62], large-scale live-cell monitoring with subcellular resolution[13,51,52,63], microbial growth detection with nanometer topographic sensitivity[14], antimicrobial susceptibility testing[14], urine sediment screening[13], differential blood count[11,64], cytometric analysis[13,52], optofluidic ptychographic screening[65] and depth-multiplexed imaging of stacked biosamples on a chip[63], among others.

Despite these many benefits, there are also several limitations associated with both implementations. First, a successful reconstruction in FP and CP relies on an accurate imaging model of the system. With FP, the imaging model discussed in Fig. 2 (the product between the object and the plane wave) assumes that the object section is infinitesimally thin. For any practical specimen with a certain thickness, tilting the illumination plane wave would also change the object spectrum in addition to shifting it in the Fourier space. Therefore, it is challenging for FP to image 3D thick samples such as an optical lens or a large bacterial colony. While it is possible to partially address this issue by implementing diffraction tomography[19] or multislice modeling[66] in FP, the resulting computational cost may still be prohibitively high for biomedical researchers. In contrast, CP recovers the object exit wavefront at the blood-cell layer plane, avoiding the direct modeling of the light–object interaction process, and so is better suited to imaging thick specimens. This has been demonstrated by imaging inch-size optical lenses, large bacterial colonies and thick cytology smears from fine needle aspiration[11,12,14]. By integrating CP with multislice modeling, it is also possible to image multiple stacked biosamples on a chip[63].

Second, the LED light source used in FP has a low optical flux. A longer exposure time is often required to achieve an adequate signal-to-noise ratio when capturing darkfield images. The laser source for CP, on the other hand, has a high optical flux for a much shorter exposure time, allowing continuous sample motion during the image acquisition process. The laser source in CP, however, introduces coherent artefacts to the captured images. One prominent artifact is the interference fringe pattern caused by multiple reflections between different glass–air interfaces. To reduce the impact of this artifact, we can use a dense monolayer of blood cells on the image sensor and increase the number of acquisitions. Another solution is to coat a thin light-absorbing layer on the sensor's coverglass. Light beams undergoing multiple reflections will be absorbed multiple times, thereby minimizing the coherent artifacts. The third solution is to use a laser with low spatial coherence but high temporal coherence. Such a light source could be the optimal choice for both FP and CP.

Third, both FP and CP are coherent imaging modalities. Their native forms cannot be used for incoherent fluorescence imaging, although it is possible to extend the concepts for incoherent imaging, in a way similar to SIM[67–70].

Fourth, in a time-lapse experiment, both FP and CP necessitate substantial computational resources for storing, transferring and processing a large amount of data (measured in terabytes). One strategy is to alleviate this is take advantage of the temporal correlation of the specimens and reduce the number of acquisitions by using the reconstruction from the previous timepoint as the initial guess of the current timepoint[14,65].

Fifth, the distance between the object and the coded sensor is often less than 1 mm in CP. Therefore, the heat generated by the sensor may affect the specimen, especially for cell culture experiments. We can use heatsinks and small fans to partially address this issue. However, this passive solution is suboptimal as the temperature of the coded sensor surface is still higher than that of the surrounding environment. If the temperature is a critical consideration for the experiment, active thermoelectric cooling and temperature sensor feedback are needed for heat management, which is beyond the scope of this protocol.

Overview of the procedure

Figure 3 shows the overall workflow of this protocol: Procedure 1 in the left panel covers the FP system and Procedure 2 in the right panel covers the CP system. Procedure 1 for the FP system begins with the development of a programmable light source (Steps 1–8, Procedure 1). We discuss two designs of the light source: (1) a custom planar LED matrix built with small-pitch surface mount elements and (2) an assembled planar LED array built with off-the-shelf LED matrixes. Next, the light source module is attached to a regular light microscope for system integration (Steps 9–27, Procedure 1). With a properly aligned LED source, we discuss two options to calibrate the incident angles of different LED elements (Steps 28–43, Procedure 1). The first option relies on the brightfield-to-darkfield transition features of the captured image and can be used to calibrate the LED matrix with a well-defined grid pattern (Box 1 and Fig. 4). The second option is to place a calibration target at a defocused plane and use a high-NA objective lens to acquire a set of images under illumination with different LED elements. Cross-correlation analysis is then performed to obtain the incident angle information from the captured images. This second angle-calibration option can be used for any planar LED illuminator. Next, we calibrate the pupil aberration of the objective lens (Steps 44–51, Procedure 1). In this process, we use a blood smear slide as the calibration object and acquire a set of images under illumination with different LED elements. The pupil aberration is then jointly recovered with the calibration object. Once the system is fully calibrated, FP imaging experiments can run for different biospecimens (Steps 52–60, Procedure 1). Two approaches are adopted to shorten the acquisition time: (1) different camera gains are applied according to the illumination NAs and (2) a portion of the LED elements are skipped in the acquisition process.

Procedure 2 for the CP system begins with the preparation of the blood-cell layer on the image sensor (Steps 1–8, Procedure 2). A good CP imaging result can be obtained with a dense and uniform monolayer of goat blood cells on the sensor. Next, the development of a motorized stage for sensor translation is discussed (Steps 9–21, Procedure 2). A low-cost *XYZ* three-axis stage is modified by

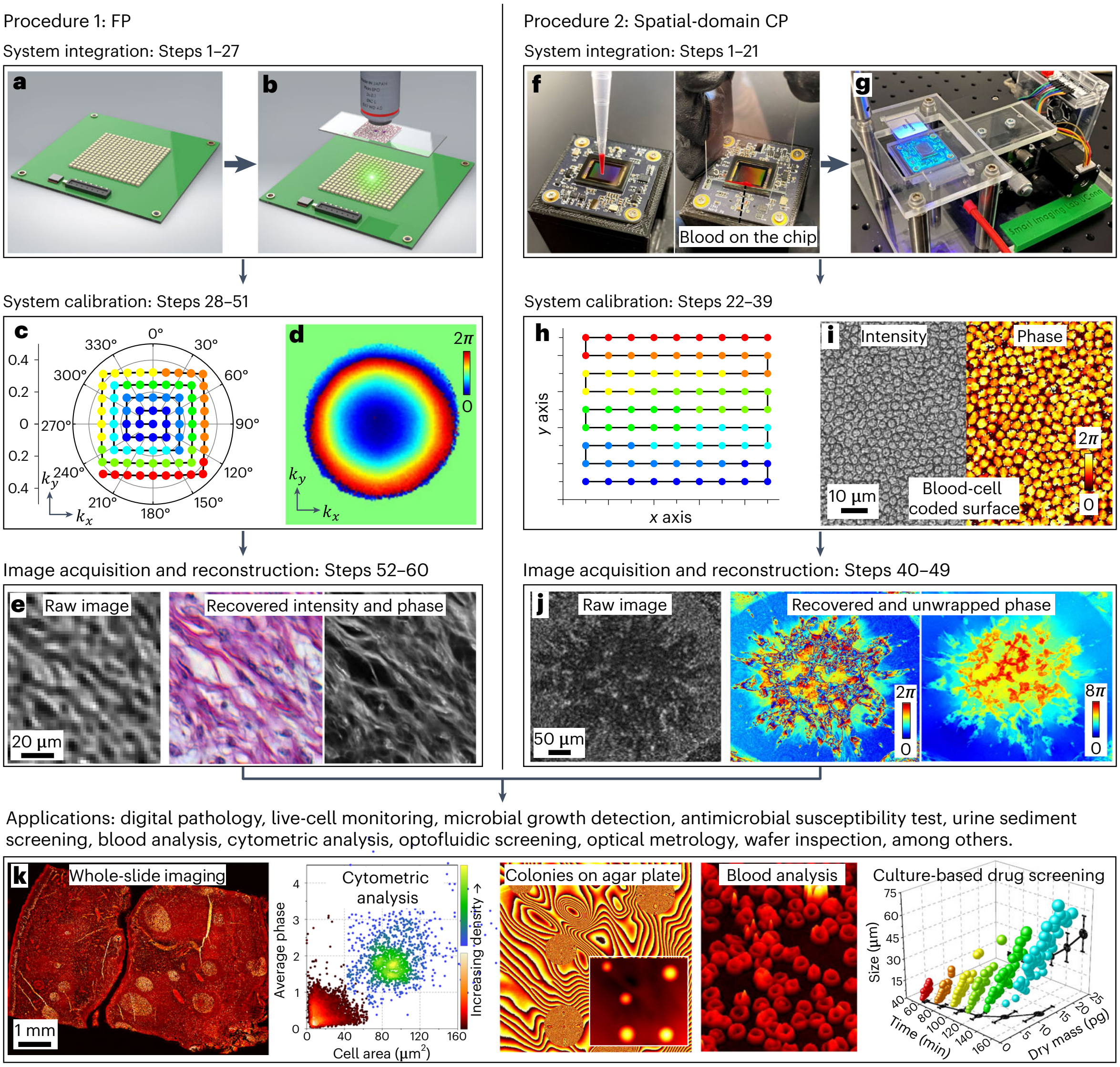

Fig. 3 | Overview of Procedures 1 and 2 for developing the FP and CP platforms. a, Programable light source development for FP. **b**, System integration and alignment for FP. **c**, Incident angle calibration for FP. **d**, Recovery of the ptychographic probe (pupil) for FP. **e**, Image acquisition and reconstruction for FP. **f**, Preparation of the blood-coated surface for CP. **g**, Motorized stage development and system integration for CP. **h**, Estimation of the scanning positions for CP. **i**, Recovery of the ptychographic probe (coded surface) for CP. **j**, Image acquisition and reconstruction for CP. **k**, Selected bio-imaging applications for both implementations. **k** adapted with permission from ref. [13], American Chemical Society, and ref. [14], Elsevier.

replacing its x and y manual actuators with stepper motors. Once the hardware development is completed, system calibration using a blood smear slide as the calibration object is described (Steps 22–39, Procedure 2). The goal of this calibration process is to recover the transmission profile of the blood-cell coded layer on the image sensor. In this calibration experiment, we scan the coded sensor to different lateral positions and acquire the corresponding images for the joint recovery of the coded layer and the calibration object. The positional shift of the coded sensor is obtained using an iterative correlation-analysis approach (Box 2). With the recovered coded layer profile, CP imaging experiments can then be run for different biospecimens (Steps 40–49, Procedure 2).

Experimental design

Hardware implementation of FP

We consider the following four experimental aspects for developing the FP setup (an FP setup built using a regular upright microscope (Nikon, Eclipse Ci) and a programmable LED array is shown in Fig. 5).

Box 1 | Incident angle calibration and alignment for FP

We discuss two approaches for obtaining the incident wavevectors of different LED elements. The first is for the planar LED matrix with a well-defined pitch and the second is for planar LED elements arranged at arbitrary 2D locations. In the first approach, we use a blank glass slide as the object and visually select an LED element underneath the blank glass slide as the reference point. On the basis of this reference point, we then select four adjacent centrosymmetric LEDs such that their incident angles are close to the maximum acceptance angle of the objective lens. By turning on these four LEDs, the captured image in Fig. 4a exhibits centrosymmetric brightfield-to-darkfield transition features[15]. To facilitate the alignment process, we display a cross marker on top of the captured image in Fig. 4a. The position of the LED matrix can be adjusted so that the brightfield-to-darkfield transition features are aligned with the cross marker. The spatial position (x_i,y_i)s of different LED elements can then be calculated on the basis of the pitch of the matrix and the detector pixel size at the object plane. The red dots in Fig. 4a denote the recovered positions of the LED elements with respect to the reference point at the center. For a given position (x_c,y_c) on the captured image, the incident wavevector (k_{xi}, k_{yi}) can be calculated via:

$$(k_{xi}, k_{yi}) = \frac{2\pi}{\lambda} \times \left(\frac{(x_c - x_i)}{\sqrt{(x_c - x_i)^2 + (y_c - y_i)^2 + h^2}}, \frac{(y_c - y_i)}{\sqrt{(x_c - x_i)^2 + (y_c - y_i)^2 + h^2}} \right), \tag{1}$$

where h is the measured distance between the object and the planner LED matrix. Figure 4b shows the recovered wavevectors of the planar LED matrix in Fig. 5b.

In the second approach, we use a high-NA objective lens to infer the incident wavevectors of the freeform LED elements located at arbitrary 2D positions[88]. First, we place a calibration target (e.g., a blood smear slide) at an out-of-focus plane with a defocused distance Δz. We then select and turn on a reference LED element underneath the sample and capture the corresponding image $I_{\mathrm{ref}}(x,y)$. Second, a set of defocused images $I_i(x,y)$ $(i = 1,2,3\ldots)$ are captured by turning on different LED elements of the LED illuminator. As shown in Fig. 4c, we crop the central regions of both I_{ref} and I_i to estimate the positional shift $(\Delta x_i, \Delta y_i)$ between them:

$$(\Delta x_i, \Delta y_i) = \arg\max_{(x,y)} \left\{ I_{\mathrm{ref}}^{\mathrm{crop}} \star I_i^{\mathrm{crop}} \right\}(x, y), \tag{2}$$

where '★' denotes the cross-correlation operation. On the basis of Fig. 4d, the spatial location (x_i, y_i) of the ith LED element can be obtained via

$$(x_i, y_i) = \frac{h}{\Delta z}(\Delta x_i, \Delta y_i) \tag{3}$$

The incident wavevector (k_{xi}, k_{yi}) of this element can then be calculated by equation (1), and Fig. 4e shows the recovered wavevectors of the illuminator in Fig. 5c.

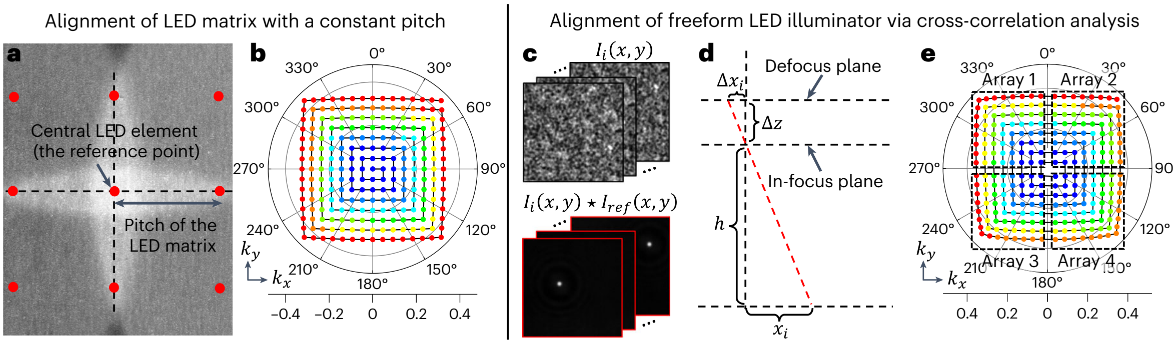

Fig. 4 | Incident angle calibration and alignment for FP. a, Alignment of a planar LED matrix with a constant pitch. **b**, The recovered wavevectors of the planar LED matrix. **c**, The captured raw images of different LED elements and the corresponding correlation maps. **d**, Estimation of the LED position (x_i,y_i) via the positional shift $(\Delta x_i,\Delta y_i)$ from the cross-correlation analysis. **e**, The recovered wavevectors of the freeform planar LED illuminator.

Microscope selection for FP: an upright microscope system can be configured to image a biospecimen mounted on a regular microscope slide. For imaging cell cultures on a Petri dish or multiwell plate, an inverted microscope can be used instead[20,60,61].

Objective lens selection for FP: if the targeted application is to perform large-field-of-view imaging, we recommend the following low-NA objective lenses: (1) 2×, 0.1 NA objective lens (Nikon, Plan Apo), (2) 4×, 0.2 NA objective lens (Nikon, Plan Apo), (3) 2×, 0.1 NA objective lens (Thorlabs, TL2X-SAP) and (4) 4×, 0.2 NA objective lens (Thorlabs, TL4X-SAP). If the targeted application is to push the resolution limit to the theoretical maximum[38,71,72], one can choose an objective lens with a high NA, for example, a 40×, 0.95 NA objective lens in free space (Nikon, Plan Apo).

Box 2 | Tracking the motion of the coded sensor in CP

In the image acquisition process, CP translates the blood-coated sensor to different *x*-*y* positions and records a set of intensity images $I_i(x'', y'')s(i = 1, 2, \ldots)$ of the object. The translated positions of the coded sensor need to be recovered for the subsequent reconstruction process. The captured images, however, contain information about both the object and the coded surface. To track the positional shift of the coded sensor, we need to minimize the impact of the coded surface. Since the coded surface remains stationary during the sensor translation process, the modulation effect can be approximated by the sum of all measurements $\sum_{t=1}^{T} I_t(x'', y'')$. Dividing this term can thus effectively reduce the modulation effect of the coded surface[50]:

$$I_i'(x'', y'') = I_i(x'', y'') / \sum_{t=1}^{T} I_t(x'', y'') \tag{4}$$

If we use the first image as the reference, the translational shift between the first and the *i*th image (x_i,y_i) can be estimated by locating the maximum point of the following cross-correlation map (Fig. 8a):

$$(x_i, y_i) = \arg\max_{(x'', y'')} \left\{ I_i' \star I_1' \right\}(x'', y'') \tag{5}$$

where '★' denotes the cross-correlation operation. With the initially estimated shifts (x_i,y_i) in Fig. 8b, a reference image can be generated as follows (Fig. 8c):

$$I_{\mathrm{ref}}(x'', y'') = \sum_{i=1}^{T} I_i'(x'' + x_i, y'' + y_i), \tag{6}$$

where the measurements are shifted back to the first translated position and summed to remove the modulation effect of the coded surface. This reference image then replaces the term I_1' in equation (5) for generating a set of updated positional shifts (x_i,y_i)s. The correlation analysis procedures of equations (5) and (6) are typically repeated one to three times to obtain a motion estimate of the coded sensor with deep subpixel accuracy[50] (Fig. 8c).

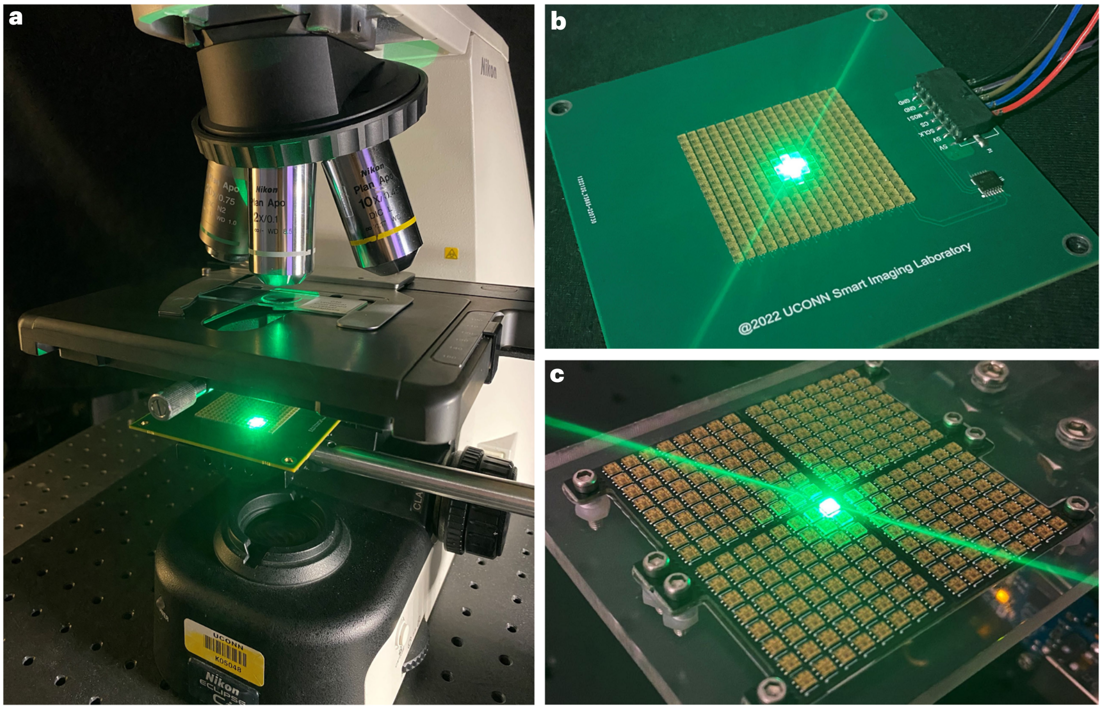

Fig. 5 | Hardware implementation of FP. a, An FP setup built with an LED illuminator and an upright microscope with a 2×, 0.1 NA objective lens. **b**,**c**, Two designs of the LED illuminator: a custom-made planar LED matrix built with small-pitch surface mount elements (**b**), and an assembled planar LED array built with off-the-shelf LED boards (**c**). By turning on different LED elements on the array, the system records a set of low-resolution object images corresponding to different incident angles. These captured images are then used to recover the high-resolution object with both intensity and phase properties. Also refer to Supplementary Video 1 for the operation of the FP platform.

Camera selection for FP: we recommend choosing the camera pixel size for FP[73] according to the following formula:

$$\frac{\lambda \times \mathrm{Mag}}{4 \times \mathrm{NA_{obj}}} \leq \text{Sampling pixel size} \leq \frac{\lambda \times \mathrm{Mag}}{2 \times \mathrm{NA_{obj}}}, \tag{7}$$

where Mag is the magnification factor of the microscope system, $\mathrm{NA_{obj}}$ is the NA of the objective lens and λ is the illumination wavelength. The right-hand side of equation (7) is the sampling condition for the coherent imaging system. If the camera pixel size is larger than this limit, it will cause aliasing issues for the measurements and require a subsampling scheme in the phase retrieval process. The left-hand side of equation (7) comes from the sampling condition for the incoherent imaging system. A pixel size smaller than this limit leads to data redundancy: no additional object information can be obtained compared with the image captured using a pixel size of $(\lambda\times\mathrm{Mag})/(4\times\mathrm{NA_{obj}})$. Instead, a smaller pixel size than this limit often implies a lower full well capacity of the pixel and a higher level of noise. For the FP system discussed in this protocol, we have $\lambda = 470$ nm, Mag = 2 and $\mathrm{NA_{obj}} = 0.1$, giving a preferred pixel size from 2.34 µm to 4.7 µm according to equation (7). To this end, we recommend a low-cost 20-megapixel camera with a 2.4 µm pixel size (Sony IMX 183, model no. DMK 33UX183, The Imaging Source, ~US$700). The relatively small pixel size of this sensor assures adequate sampling for most FP configurations. If budget allows, other large-format, high-pixel-count cameras can also be used, for example, Sony IMX 540 (24.5 megapixels, 2.75 µm pixel size, model no. BFS-U3-244S8M-C, Teledyne FLIR, ~US$2,600).

Illuminator selection for FP: we recommend using small and bright surface-mounted LED elements for building the illuminator. For the same illuminator-to-sample distance, a smaller pitch implies a larger spectrum overlap in the Fourier space, thereby enabling a well-constrained and faster FP construction process. One can also bring the illuminator closer to the object to increase the optical flux per area. Other effective illuminators for FP include dome-shape LED arrays[74,75] and LED ring array[76]. Figure 4b,c shows two different planar LED illuminators discussed in this protocol.

Software implementation of FP

A successful FP reconstruction relies on accurate estimation of the illumination angle and recovery of the spatially variant pupil aberration. Box 1 discusses how to obtain the incident wavevectors of different LED elements using a calibration experiment. Further refinement of the incident wavevectors can be performed in the iterative phase retrieval process[77]. For pupil aperture recovery, we model the pupil aberration as a summation of different Zernike modes as follows:

$$\mathrm{Pupil}(k_x, k_y) = \mathrm{circ}\left(\mathrm{NA}\cdot\frac{2\pi}{\lambda}\right)\cdot\exp\left(i\cdot\sum_{n=1}^{N} w_n \cdot Z_n(k_x, k_y)\right) \tag{8}$$

where circ(NA·2π/λ) represents a circular mask with a radius of NA·2π/λ, corresponding to the aperture size of the microscope system. The term Z_n (k_x,k_y) in equation (8) represents the nth Zernike mode and w_n represents the weight of this mode. In the pupil calibration experiment, we use a blood smear as the calibration object and recover the weight w_n via gradient descent[36]. Once the weights $w_n(n = 1,2,\ldots)$ are recovered from the calibration experiment, we can generate the corresponding pupil using equation (8) and use it as the initial pupil for all subsequent imaging experiments. Figure 6 shows the reconstruction pipeline of the FP approach. It consists of three major steps: object initialization, iterative reconstruction and postprocessing transformation. To further refine the pupil aberration, we can jointly update the object and pupil using the rPIE algorithm[78] in lines 11–12 of Fig. 6. The intensity variation of the captured image can be corrected in the iterative phase retrieval process[79]. Other effective algorithms for object and pupil update include the second-order Gauss–Newton method[77] and first-order altering direction methods of multipliers[80], among others[6].

Hardware implementation of CP

Figure 7a shows a CP setup built using a blood-coated image sensor, a modified low-cost motorized stage and a fiber-coupled laser light source. We consider the following three experimental aspects for developing the CP setup.

Blood-coated image sensor for CP: the selection of the image sensor is critical to the image quality of the CP reconstruction. We recommend a monochrome image sensor with a pixel size of 1.85 µm in this protocol (Sony IMX 226, The Imaging Source, DMM 37UX226). Other sensors with smaller pixel sizes can also be selected for implementing CP. Figure 7b,c provides two options for preparing the

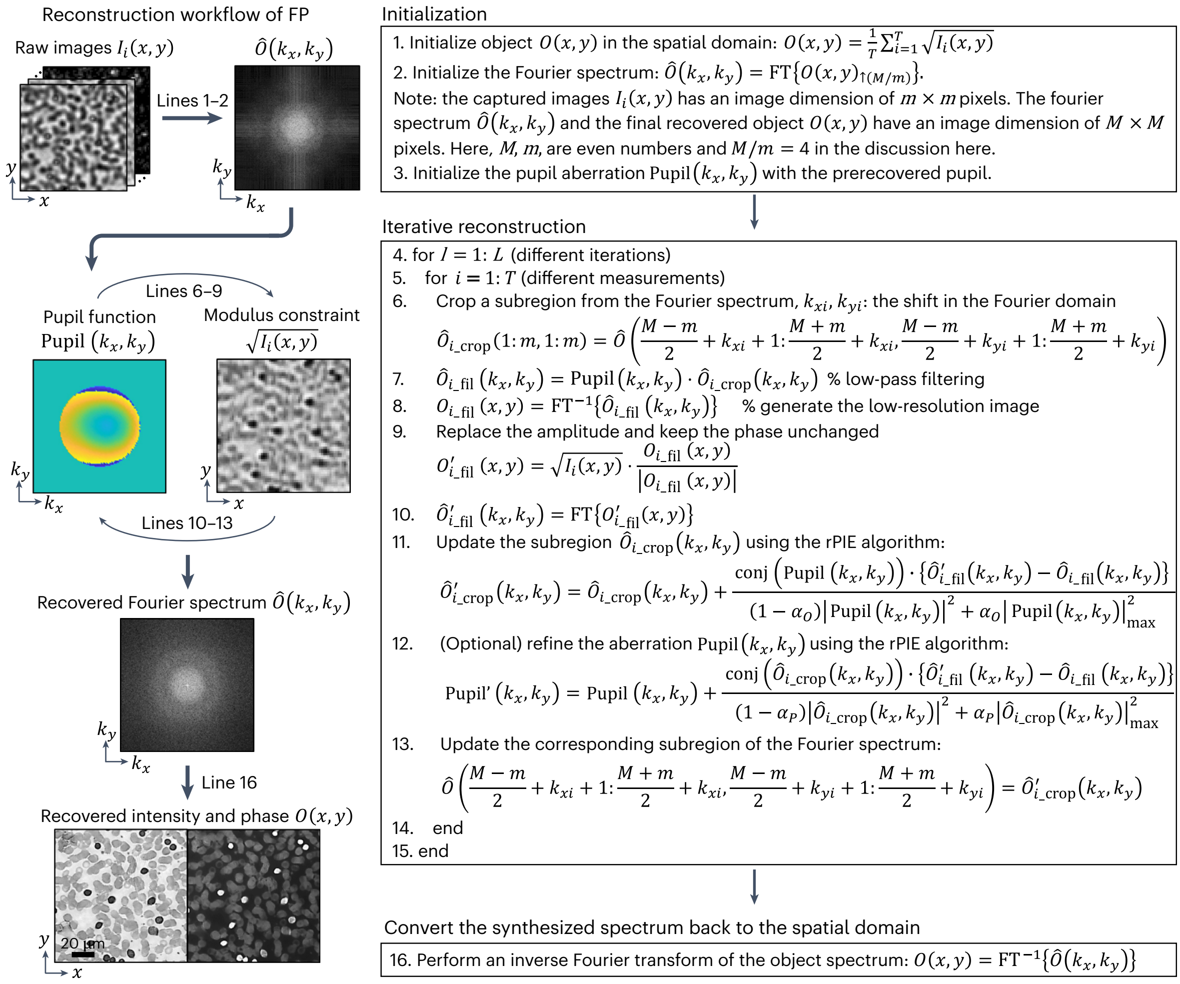

```
Initialization
1. Initialize object $O(x,y)$ in the spatial domain: $O(x,y) = \frac{1}{T}\sum_{i=1}^{T}\sqrt{I_i(x,y)}$
2. Initialize the Fourier spectrum: $\hat{O}(k_x,k_y) = \mathrm{FT}\{O(x,y)_{\uparrow(M/m)}\}$.
Note: the captured images $I_i(x,y)$ has an image dimension of $m \times m$ pixels. The fourier spectrum $\hat{O}(k_x,k_y)$ and the final recovered object $O(x,y)$ have an image dimension of $M \times M$ pixels. Here, $M$, $m$, are even numbers and $M/m = 4$ in the discussion here.
3. Initialize the pupil aberration Pupil$(k_x,k_y)$ with the prerecovered pupil.

Iterative reconstruction
4. for $l = 1{:}\,L$ (different iterations)
5.   for $i = 1{:}\,T$ (different measurements)
6.     Crop a subregion from the Fourier spectrum, $k_{xi}$, $k_{yi}$: the shift in the Fourier domain
       $\hat{O}_{i\_crop}(1{:}m, 1{:}m) = \hat{O}\left(\frac{M-m}{2}+k_{xi}+1{:}\frac{M+m}{2}+k_{xi}, \frac{M-m}{2}+k_{yi}+1{:}\frac{M+m}{2}+k_{yi}\right)$
7.     $\hat{O}_{i\_fil}(k_x,k_y) = \mathrm{Pupil}(k_x,k_y)\cdot\hat{O}_{i\_crop}(k_x,k_y)$ % low-pass filtering
8.     $O_{i\_fil}(x,y) = \mathrm{FT}^{-1}\{\hat{O}_{i\_fil}(k_x,k_y)\}$ % generate the low-resolution image
9.     Replace the amplitude and keep the phase unchanged
       $O'_{i\_fil}(x,y) = \sqrt{I_i(x,y)}\cdot\frac{O_{i\_fil}(x,y)}{|O_{i\_fil}(x,y)|}$
10.    $\hat{O}'_{i\_fil}(k_x,k_y) = \mathrm{FT}\{O'_{i\_fil}(x,y)\}$
11.    Update the subregion $\hat{O}_{i\_crop}(k_x,k_y)$ using the rPIE algorithm:
       $\hat{O}'_{i\_crop}(k_x,k_y) = \hat{O}_{i\_crop}(k_x,k_y) + \frac{\mathrm{conj}(\mathrm{Pupil}(k_x,k_y))\cdot\{\hat{O}'_{i\_fil}(k_x,k_y)-\hat{O}_{i\_fil}(k_x,k_y)\}}{(1-\alpha_O)|\mathrm{Pupil}(k_x,k_y)|^2+\alpha_O|\mathrm{Pupil}(k_x,k_y)|^2_{\max}}$
12.    (Optional) refine the aberration Pupil$(k_x,k_y)$ using the rPIE algorithm:
       $\mathrm{Pupil}'(k_x,k_y) = \mathrm{Pupil}(k_x,k_y) + \frac{\mathrm{conj}(\hat{O}_{i\_crop}(k_x,k_y))\cdot\{\hat{O}'_{i\_fil}(k_x,k_y)-\hat{O}_{i\_fil}(k_x,k_y)\}}{(1-\alpha_P)|\hat{O}_{i\_crop}(k_x,k_y)|^2+\alpha_P|\hat{O}_{i\_crop}(k_x,k_y)|^2_{\max}}$
13.    Update the corresponding subregion of the Fourier spectrum:
       $\hat{O}\left(\frac{M-m}{2}+k_{xi}+1{:}\frac{M+m}{2}+k_{xi}, \frac{M-m}{2}+k_{yi}+1{:}\frac{M+m}{2}+k_{yi}\right) = \hat{O}'_{i\_crop}(k_x,k_y)$
14.  end
15. end

Convert the synthesized spectrum back to the spatial domain
16. Perform an inverse Fourier transform of the object spectrum: $O(x,y) = \mathrm{FT}^{-1}\{\hat{O}(k_x,k_y)\}$
```

Fig. 6 | Reconstruction process of FP. Left: the workflow of the FP reconstruction process. Right: the detailed reconstruction process consists of initialization, iterative reconstruction and image transformation steps.

blood-coated surface on the image sensor. We recommend using goat blood as it can be purchased at a low cost and has the smallest blood cell size (of 2–3 µm) among all animals. An alternative to this blood-cell layer is the disorder-engineered surface with both phase scatters and intensity absorbers[11].

Mechanical stage selection for CP: we choose a low-cost *XYZ* three-axis manual stage for the CP setup. As shown in Fig. 7a, the *x* and *y* manual actuators are replaced by two stepper motors for motorized control. The *z* actuator allows users to adjust the distance between the coded sensor and the specimen. The scanning positions of the modified motorized stage can be inferred from the captured raw images (Fig. 8), allowing open-loop operation without requiring any position feedback. However, if the sample itself does not have any feature (e.g., a blank glass slide), the positional tracking process may not work and we may need to pair another image sensor for tracking the features from the sample holder[12].

Light source selection for CP: an off-the-shelf fiber-coupled 405 nm laser is adopted for the CP setup in Fig. 7a. A low-cost alternative is to obtain a 405 nm laser diode from a Blu-ray player and couple the light to a single-mode fiber for CP[13]. Unlike the FP approach, where chromatic dispersion can be partially compensated by the lens system, the free-space propagation process in CP disperses light at different wavelengths to different axial planes of the system. This dispersion can be compensated algorithmically, using multiple mutually incoherent states to model different wavelengths within the spectrum of the low-coherence source[31,53,81].

Software implementation of CP

In parallel with the incident angle calibration process in FP, we need to estimate the positional shifts of the coded sensor during the image acquisition process. If the system does not contain the coded

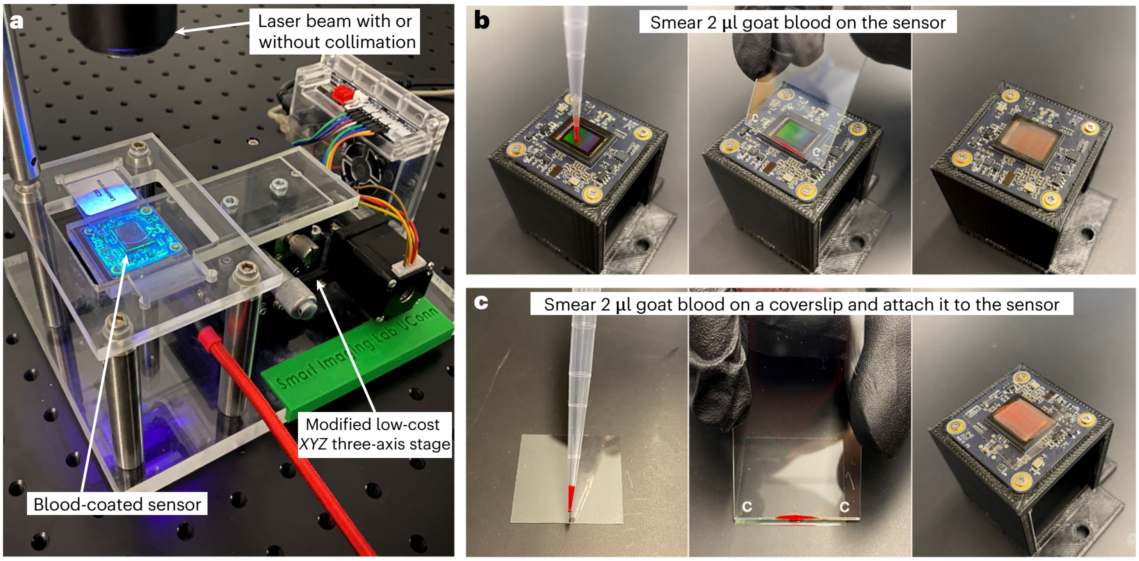

Fig. 7 | Hardware implementation of CP. a, A CP setup built with a blood-coated image sensor, a 405 nm fiber-coupled laser and a modified low-cost *XYZ* stage. The *x* and *y* manual actuators of the stage are replaced with stepper motors for motorized control. The *z* actuator is used to adjust the distance between the coded sensor and the specimen. **b**, Preparation of the blood-coated sensor by smearing 2 μl goat blood directly on top of the sensor's coverglass. **c**, Preparation of blood-coated sensor by first smearing 2 μl goat blood on a thin coverslip and then permanently attaching the coverslip to the image sensor with polydimethylsiloxane. For both **b** and **c**, we fix the cell layer with alcohol to preserve its morphology. Also refer to Supplementary Video 2 for the operation of the CP platform.

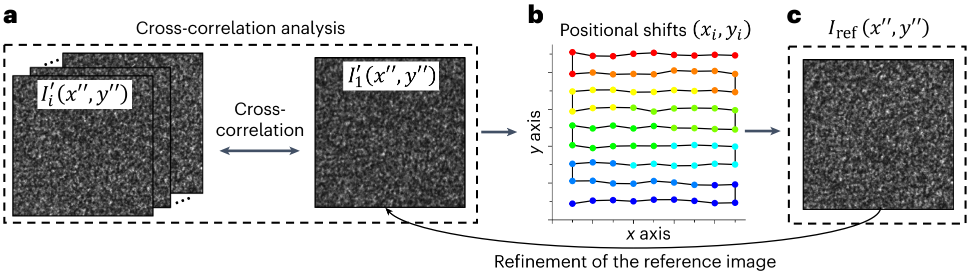

Fig. 8 | Tracking the motion of the coded sensor in CP. a, Cross-correlation analysis for positional tracking. **b**, Initially estimated positional shifts. **c**, Refinement of the positional shifts using the updated reference image.

surface, one can directly track the positional shifts via cross-correlation analysis. Box 2 discusses an iterative motion-tracking procedure that minimizes the modulation effect of the coded surface[50]. It can precisely track the positional shifts of the coded sensor with deep subpixel accuracy. In addition to the solution provided in Box 2, other alternatives can also be taken for tracking the motion of the coded sensor. For example, one can generate a clear region on the coded surface by removing parts of the blood-cell layer. Object diffraction patterns passing through this clear region can then be used for cross-correlation analysis[11,82]. A precise motorized stage with an encoder can also be adopted for hardware-based motion tracking.

In parallel with the pupil recovery process in FP, we need to recover the transmission profile of the blood-cell layer and use it as the ptychographic probe for subsequent experiments. To this end, we use a blood smear slide as the calibration object and acquire 1,500 images for the joint recovery of both the object exit wavefront and the coded surface profile at the modulation plane. Figure 9 shows the reconstruction pipeline of the CP approach, which consists of three major steps: object initialization, iterative reconstruction and postmeasurement refocusing. With the prerecovered coded surface, we then acquire ~300 raw images for each subsequent experiment, with an acquisition time of ~12 s. By using this strategy, CP can recover the phase wrapping information of different types of thick objects, including optical lens, prism, bacterial colonies on an uneven agar plate, urine crystals and cytology smears[11–13]. The phase profiles of these objects contain slow-varying contents with many 2π wraps, and they are challenging to recover using conventional lensless imaging techniques.

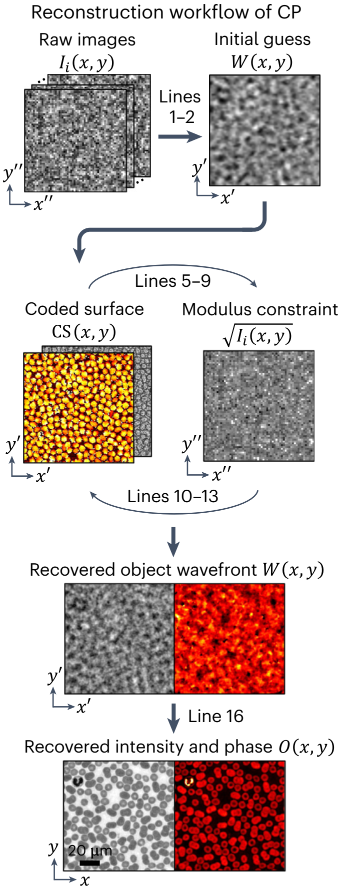

Initialization

```
1. Initialize the object wavefront $W(x,y)$ on the coded surface plane:
$W(x,y) = \mathrm{PSF}_{\mathrm{free}}(-d_2) * \left(\frac{1}{T}\sum_{i=1}^{T}\sqrt{I_i(x+x_i, y+y_i)}\right)_{\uparrow M}$
% '↑M': M-fold up-sampling; '$\mathrm{PSF}_{\mathrm{free}}$': point spread function for free space propagation
2. (Calibration only) Initialize the coded surface profile:
$\mathrm{CS}(x,y) = \mathrm{PSF}_{\mathrm{free}}(-d_2) * \left(\frac{1}{T}\sum_{i=1}^{T}\sqrt{I_i(x,y)}\right)_{\uparrow M}$
```

Iterative reconstruction

```
3. for $l = 1: L$ (different iterations)
4.     for $i = 1: T$ (different measurements)
5.     $W_{i\_\mathrm{shift}}(x,y) = W(x-x_i, y-y_i)$ % shift the wavefront based on the estimated shift
6.     $E_i(x,y) = \mathrm{CS}(x,y) \cdot W_{i\_\mathrm{shift}}(x,y)$ % exit wave at the coded surface plane
7.     $S_i(x,y) = E_i(x,y) * \mathrm{PSF}_{\mathrm{pixel}}(d_2)$ % propagate the exit wave to the sensor plane
8.     Down-sample the intensity image on the sensor plane:
       $U_i(\lceil x/M \rceil, \lceil y/M \rceil) = \left(|S_i(x,y)|^2 * \mathrm{PSF}_{\mathrm{pixel}}\right)_{\downarrow M}$
       % '⌈ ⌉': ceiling function; '↓M': M-fold down-sampling
9.     Update $S_i(x,y)$ on the sensor plane:
           $S_i'(x,y) = S_i(x,y) \cdot \frac{\sqrt{I_i(\lceil x/M \rceil, \lceil y/M \rceil)}}{\sqrt{U_i(\lceil x/M \rceil, \lceil y/M \rceil)}}$
10.    $E_i'(x,y) = S_i'(x,y) * \mathrm{PSF}_{\mathrm{free}}(-d_2)$ % propagate the field back to the coded surface plane
11.    Update the shifted object wavefront $W_{i\_\mathrm{shift}}(x,y)$ using the rPIE algorithm:
           $W_{i\_\mathrm{shift}}'(x,y) = W_{i\_\mathrm{shift}}(x,y) + \frac{\mathrm{conj}(\mathrm{CS}(x,y)) \cdot \{E_i'(x,y) - E_i(x,y)\}}{(1-\alpha_W)|\mathrm{CS}(x,y)|^2 + \alpha_W |\mathrm{CS}(x,y)|_{\max}^2}$
12.    (Calibration only) Update the coded surface profile $\mathrm{CS}(x,y)$ using the rPIE routine:
           $\mathrm{CS}'(x,y) = \mathrm{CS}(x,y) + \frac{\mathrm{conj}\left(W_{i\_\mathrm{shift}}(x,y)\right) \cdot \{E_i'(x,y) - E_i(x,y)\}}{(1-\alpha_{\mathrm{CS}})\left|W_{i\_\mathrm{shift}}(x,y)\right|^2 + \alpha_{\mathrm{CS}}\left|W_{i\_\mathrm{shift}}(x,y)\right|_{\max}^2}$
13.    $W(x,y) = W_{i\_shift}'(x+x_i, y+y_i)$ % Shift back the updated wavefront
14.    end
15. end
```

Postmeasurement refocusing

```
16. Propagate the exit wavefront back to the object plane: $O(x,y) = W(x,y) * PSF_{free}(-d_1)$
```

Fig. 9 | Reconstruction process of CP. Left: the workflow of the CP reconstruction process. Right: the detailed reconstruction process consists of initialization, iterative reconstruction and image refocusing steps. The coordinates (*x*,*y*), (*x*′,*y*′) and (*x*′′,*y*′′) are used interchangeably.

Materials for Procedure 1: FP

Equipment

- Computer with 64 GB random access memory and a graphics card (Nvidia, RTX 3090 or RTX 4090)
- Upright microscope (Nikon, ECLIPSE Ci series)
- Clamping forks (Thorlabs, model no. CF175 ×4)
- Solid aluminum optical breadboard (Thorlabs, model no. MB18)
- Camera (The Imaging Source, model no. DMK 33UX183)
- USB cable for camera connection (The Imaging Source, model no. CA-USB30-AmB-BLS)
- *XYZ* three-axis manual stage (ToAuto, model no. LD60-LM)
- Post holder (Thorlabs, model no. UPH1 ×4)
- 2×, 0.1 NA objective lens (Nikon, Plan APO)
- 20×, 0.75 NA objective lens (Nikon, Plan APO)
- Angle post clamp (Thorlabs, model no. RA90 ×1)
- Optical posts (Thorlabs, model no. TR1 ×4)
- Optical posts (Thorlabs, model no. TR3 ×2)
- Optical posts (Thorlabs, model no. TRA30/M ×2)
- Optical posts (Thorlabs, model no. TR6 ×1)
- Precision Kinematic Mirror Mount (Thorlabs, model no. KS1T ×1)
- 17 × 17 LED array (Custom order)
- 8 × 8 LED array (Adafruit, cat no. 3444 ×4)
- 200 mm × 200 mm × 6 mm acrylic sheet (custom order)
- Jumper wire (Amazon ×20)
- M2 screws (NBK, cat no. SNSS ×8)
- M4 screws (Thorlabs, model no. SH4MS06 ×2)

- M6 screws (Thorlabs, model no. SH6MS06 ×2)
- 8-32 × 3/8″ cap screws (Thorlabs, model no. SH8S025 ×6)
- 1/4″ 20 × 5/8″ cap screws (Thorlabs, model no. SH25S063 ×4)
- 8-32 × 1/2″ setscrew (Thorlabs, model no. SS8S050)
- 5 V, 2 A power source
- 12 V, 2 A power source

Tools

- 3D printer (MakerBot, model no. Replicator 2)
- Milling machine (Roland, model no. monoFab SRM-20)
- Rotary carver (Uolor, model no. UH032)
- Level (MSC, cat no. 67944728)
- Blood smear slide (Carolina, 313158)
- Microscope stage calibration slide (BoliOptics, cat no. RT20201101)

Software

- MATLAB R2022b or higher (https://www.mathworks.com/products/matlab.html)
- IC capture version 2.4 or higher (https://www.theimagingsource.com/support/downloads-for-windows/end-user-software/iccapture/)
- SOLIDWORKS 2021 or higher (https://www.solidworks.com/product/all-products)
- Arduino IDE version 1.8 or higher (https://www.arduino.cc/en/software)

Materials for Procedure 2: spatial-domain CP

Reagents

- Goat blood 50 ml (Lampire Biological Laboratories, cat no.7202501)
- Silicone (Dow, SYLGARD 184 silicone elastomer kit)

Equipment

- Computer with 64 GB random access memory and a graphics card (Nvidia, RTX 3090 or RTX 4090)
- Camera (The Imaging Source, model no. DMM 37UX226)
- USB cable for camera connection (Anker, USB 3.0 to USB C)
- Image sensor heat sink (Alpha, model no. LPD40-3B ×2)
- 22 mm × 22 mm coverslips (Thorlabs, model no. CG00C2)
- *XYZ* three-axis manual stage (ToAuto, model no. LD60-LM)
- Stepper motor (NEMA, model no.11 ×2)
- Stepper motor controller (GRBL, model no. 1.1 V3.4)
- 405 nm fiber-coupled laser (Thorlabs, model no. LP405-SF10)
- (Optional; other drivers can also be used) Laser driver (Thorlabs, model no. ITC4001)
- Laser diode mount (Thorlabs, model no. LDM9LP)
- Laser fiber adaptor (Thorlabs, model no. S120-FC)
- Optical posts (Thorlabs, model no. TR3 ×4)
- Optical posts (Thorlabs, model no. TR4)
- Optical posts (Thorlabs, model no. TR1.5)
- Angle post clamp (Thorlabs, model no. RA90)
- 1 inch extension tube slip ring (Thorlabs, model no. SM1RC)
- 1 inch optical tube (Thorlabs, model no. SM1L20)
- 2 inch 200 mm bi-convex lens (Thorlabs, model no. LB1199)
- 2 inch optical tubes (Thorlabs, model no. SM2L30 ×2)
- 2 inch optical tubes (Thorlabs, model no. SM2L05)
- 2 inch extension tube slip ring (Thorlabs, model no. SM2RC)
- 2 inch adjustable optical tube (Thorlabs, model no. SM2V15)
- Optical tube adapter (Thorlabs, model no. SM1A2)
- 250 mm × 200 mm × 12 mm acrylic sheet (custom order)
- 150 mm × 100 mm × 6 mm acrylic sheet (custom order)
- 1/4″ 20 × 1/2″ setscrews (Thorlabs, model no. SS6MS12 ×4)
- 8-32 × 3/8″ cap screws (Thorlabs model no. SH8S025 ×20)
- 8-32 × 1/2″ setscrew (Thorlabs, model no. SS8S050 ×4)

- Jumper wire (Amazon ×4)
- M2 screws (NBK, cat no. SNSS ×4)
- 24 V, 2 A power source

Tools

- 3D printer (MakerBot, model no. Replicator 2)
- Milling machine (Roland, model no. monoFab SRM-20)
- Manual driller (Delta, model no. 12 drill press)
- Rotary carver (Uolor, model no. UH032)
- 20 µl single channel pipette (Eppendorf, cat no. 3123000055)
- Vacuum desiccator (Amazon, model no. SP Bel-Art 420200000)
- Level (MSC, cat no. 67944728)
- Blood smear slide (Carolina, 313158)

Software

- MATLAB R2022b or higher (https://www.mathworks.com/products/matlab.html)
- IC capture version 2.4 or higher (https://www.theimagingsource.com/support/downloads-for-windows/end-user-software/iccapture/)
- SOLIDWORKS 2021 or higher (https://www.solidworks.com/product/all-products)
- Arduino IDE version 1.8 or higher (https://www.arduino.cc/en/software)

Procedure 1: FP

Programable light source development ● Timing 3–5 h

▲ **CRITICAL** We discuss two options for programable light source development. Steps 1–3 prepare a custom planar LED matrix with 17-by-17 LED elements. Steps 4–8 are used to prepare an assembled planar LED illuminator using four off-the-shelf LED matrixes.

1 Illuminator 1: single planar LED array (Steps 1–3). Build a customized LED board following the printed circuit board design in Supplementary Fig. 1a and Supplementary Data ‘FP_design_singleLEDarray.zip’.

2 Connect the LED board in Step 1 to an Arduino Uno microcontroller based on the pin assignment outlined in Supplementary Fig. 1b,c.

3 Upload the control code to the Arduino Uno board. The code is provided in Supplementary Software ‘FP_controlCode_SingleLEDarray.ino’.

4 Illuminator 2: assembled planar LED illuminator (Steps 4–8). Prepare four off-the-shelf LED matrixes (Adafruit, product ID: 3444). Follow Supplementary Fig. 2a to cut the edge of the LED boards and smooth the incision with a rotary carver (Uolor, UH032). Solder four jumper wires to the input pins of each LED matrix.

5 Prepare an acrylic base with 12 mounting holes: 8 holes for the 4 LED matrixes, 2 holes for the Arduino Uno board and the remaining 2 for attaching to a XYZ three-axis manual stage (ToAuto, LD60-LM). The design file for the acrylic base is provided in Supplementary Data ‘FP_4LEDholder.SLDPRT’.

6 Attach the four LED matrixes on the acrylic base using eight M2 screws, as shown in Supplementary Fig. 2b1.

7 Connect the jumper wires from the LED matrixes to the Arduino Uno board according to Supplementary Fig. 2b2.

8 Upload the control code to the Arduino Uno board. The code is provided in Supplementary Software ‘FP_controlCode_Adafruit_DotStar.ino’.

System integration and alignment ● Timing 1–2 h

▲ **CRITICAL** A proper optical alignment can facilitate the calibration process of FP. In this section, we explain how to align the LED illuminator with respect to the camera. For a planar LED matrix with a constant pitch, we use the brightfield-to-darkfield transition features for system alignment. For other planar freeform illuminators (e.g., Fig. 5c), we use a blood smear slide as a calibration object for system alignment.

9 Install MATLAB and the Image Acquisition Toolbox on a computer.

10 Install IC Capture software and the driver for the 33U series (version 5.1.0.1719) of the camera (The Imaging Source, DMK 33UX183).

11 Install CUDA driver (CUDA Toolkit v11.7) for the Nvidia graphics card.

12 System integration (Steps 12–16). Prepare an optical breadboard (Thorlabs, MB18) as the base for the FP system.

13 Mount the microscope (Nikon, Eclipse Ci-S) on the optical breadboard using four clamping forks (Thorlabs, CF175). Mount the 2×, 0.1 NA objective lens (Nikon, Plan APO) and the 20×, 0.75 NA objective lens to the microscope.

14 Mount the *XYZ* three-axis manual stage on the optical breadboard using four optical posts (Thorlabs, TR1) and four post holders (Thorlabs, UPH1).

15 Mount the LED illuminator on the *XYZ* three-axis manual stage. Use the *XY* stage to translate the illuminator laterally so that the central element of the illuminator is visually under the objective lens. Use the *Z* stage to adjust the distance between the illuminator and the sample stage to be ~5 cm.

? TROUBLESHOOTING

16 Mount the camera to the photo port of the Nikon microscope. Connect the camera to the computer with the USB 3.0 cable (The Imaging Source, CA-USB30-AmB-BLS).

▲ CRITICAL STEP The camera needs to be connected to a USB 3.0 port (or above) of the computer. If connected to a USB 2.0 port, the camera cannot be operated at its maximum framerate.

17 System alignment for a planar LED matrix with a well-defined pitch (Steps 17–22). Use a level to check whether the planar illuminator is in parallel with the sample stage. If needed, attach the illuminator to a precision kinematic mirror mount (Thorlabs, KS1T) and then mount the mirror mount on the *XYZ* three-axis manual stage.

18 Put the 2×, 0.1 NA objective lens in place for system alignment.

19 Use a blank glass slide as the sample and select an LED element at the center of the illuminator as the reference point. Turn on four adjacent centrosymmetric LED elements for system alignment.

▲ CRITICAL STEP The four centrosymmetric LEDs are chosen so that their incident angles are close to the maximum acceptance angle of the objective. As a result, the captured image corresponding to these four LEDs exhibits centrosymmetric brightfield-to-darkfield transition features. A dashed cross marker from these features can then be used to align the LED matrix, as shown in Fig. 4a.

20 Initialize the image sensor, generate a cross pattern on the captured image and display it on the computer screen. The related code is provided in lines 29–55 in Supplementary Software 'FP_imageAcquisition.m'.

21 Adjust the position of the LED matrix so that the cross pattern overlaps with the brightfield-to-darkfield transition features of the captured image (Box 1).

? TROUBLESHOOTING

22 Turn off all the LEDs.

23 System alignment for nonperiodic illuminators (Steps 23–27). Put the 2×, 0.1 NA objective lens in place for system alignment. Place a blood smear slide (Carolina, 313158) on the sample stage.

24 Turn on the central LED element of the illuminator for sample illumination. Open the IC Capture software.

25 Adjust the exposure time in the IC Capture software. Adjust the focus knob to bring the sample into focus.

26 Adjust the focus knob to bring the sample to different defocus planes. Translate the LED illuminator using the *XYZ* manual stage. This step is completed if the blood smear image does not shift laterally when the blood smear is moved to a defocus plane.

27 Turn off the LED and close the IC Capture software.

Incident angle calibration ● Timing 0.5–1 h

▲ CRITICAL As discussed in Box 1, two approaches are provided for obtaining the incident wavevectors of different LED elements. The first one (Steps 33–35) is for planar LED matrixes with a well-defined pitch and the second (Steps 36–43) is for planar LED array arranged at arbitrary 2D locations.

28 Turn on the reference LED element of the illuminator and open the IC Capture software.

29 Infer the magnification factor of the 2× objective lens (Steps 29–32). Place the length calibration slide (BoliOptics, RT20201101) on the sample stage. The slide contains 101 grid lines and the distance between adjacent grid lines is 10 µm. The distance between the first and the last grid lines is 1 mm.

30 Bring the slide to the center of the camera field of view. Adjust the focus knob to bring the captured image into focus.

31 Align the orientation of the grid lines to the vertical direction of the captured image.

32 Measure the number of pixels across the 1 mm width of all grid lines. Calculate the magnification factor of the objective lens: mag = (pSize × pNum)/(1 mm), where 'pSize' represents the pixel size of the camera (2.4 μm) and 'pNum' represents the measured pixel number covering the width of all grid lines. The measured magnification factor is usually slightly different from the value labeled on the objective lens.

? TROUBLESHOOTING

33 Incident angle calibration for planer LED matrix with a well-defined pitch (Steps 33–35). Place the blood smear slide on the sample stage and adjust the focus knob to bring the captured image into focus.

34 Measure the distance between the sample and the LED board using a ruler.

▲CRITICAL STEP If needed, we can test different distance values in the FP reconstruction process and select the one with the best reconstruction quality.

35 Calculate the incident wavevector based on the LED position and the distance between the sample (Box 1). The related code is provided in Supplementary Software 'FP_calibrateAngle.m'.

▲CRITICAL STEP We assume the central position of the field of view is (0, 0). For different regions of the field of view, the incident wavevector will be different according to equation (1).

36 Incident angle calibration for non-periodic illuminators (Steps 36–43). Put the 20×, 0.75 NA objective lens (Nikon, Plan APO) in place for the calibration process.

▲CRITICAL STEP A high-NA objective lens is used so that all incident angles of the LED elements are within the detection NA of the lens. Other high-NA objective lenses can also be used here.

37 Place the blood smear slide on the sample stage and adjust the focus knob to bring the captured image into focus. Move the sample stage towards the objective lens by 80 μm. Close the IC Capture software.

▲CRITICAL STEP Each division on the fine focus knob represents a 1 μm shift in the axial direction. If the defocus distance is too short, the lateral shift induced by different LED elements will be too small for accurate incident angle estimation. If the defocus distance is too large, the defocus effect would compromise the correlation analysis process. A distance of 80 μm is a good choice considering these factors.

▲CRITICAL STEP Close the IC Capture software before running any MATLAB code that includes camera communication commands.

38 Adjust the exposure time. The related code is provided in lines 63–75 in Supplementary Software 'FP_imageAcquisition.m'.

▲CRITICAL STEP The percentage of overexposed pixels will be printed in the command window using the provided code. We recommend setting an exposure time so that the ratio of overexposed pixels is 0.01%.

39 Capture a reference image 'referenceImg'. Turn off the central LED element of the illuminator.

40 Turn on all LEDs sequentially and capture a set of images 'imageCalibration'.

41 Crop the central 1,024 × 1,024 pixel region from the reference image 'referenceImg' captured in Step 39 to obtain 'referenceCrop'. Crop the same region from 'imageCalibration' captured in Step 40 to obtain 'imageCrop'. Estimate the positional shift between the cropped image 'imageCrop' and the cropped reference image 'referenceCrop' using the function 'dftregistration'[83].

42 Calculate the 2D positions of light source elements based on the defocused distance and the estimated shifts obtained in Steps 40 and 41. Refer to Box 1 for the detailed discussion. The related code is provided in the Supplementary Software 'FP_estimate2DpositionLed.m'.

43 Calculate the incident wavevectors of different elements based on the 2D positions obtained from Step 42. Refer to Box 1 for the detailed discussion. The related code is provided in Supplementary Software 'FP_calibrateAngle.m'.

Recover the pupil aberration ● Timing 2–3 h

▲CRITICAL In this section, we discuss how to acquire a calibration dataset to recover the pupil aberration of the FP platform. Since it is a one-time process, the acquisition time does not need to be optimized. In our implementation, we set a long exposure time for darkfield image acquisition and sequentially turn on all LED elements for increasing the data redundancy of the ptychographic dataset.

44 Put the 2×, 0.1 NA objective lens in place for image acquisition.

45 Put the calibration blood smear slide on the sample stage. Turn on the reference LED. Open the IC Capture software. Adjust the focus knob to bring the image into focus. Close the IC Capture software.

▲**CRITICAL STEP** In the calibration experiment, we recommend using a thin and uniform sample with rich spatial details. The blood smear slide is an ideal choice. An improper calibration sample (e.g., a sparse sample) may lead to failure of the joint object–pupil recovery process.

46 Adjust the exposure time as in Step 38. Sequentially turn on all LEDs for image acquisition. The related code is provided in lines 91–137 in Supplementary Software 'FP_imageAcquisition.m' (under the 'calibration' mode).

▲**CRITICAL STEP** To reduce the impact of the limited dynamic range of the camera, we repeat the acquisition process with three different exposure times.

▲**CRITICAL STEP** We recommend using a dark room to minimize the impact of ambient light.

47 Process the three sets of images from Step 46 via high dynamic range (HDR) combination. The related code is provided in Supplementary Software 'FP_hdrCombine.m'. The combined HDR images are divided into segments with 256-by-256 pixels. For each small segment, the region containing brightfield-to-darkfield transition features is excluded from the dataset.

? TROUBLESHOOTING

48 Define the system parameters in MATLAB, including the NA, the magnification factor of the objective lens, the illumination wavelength, the camera pixel size and the final desired pixel size of the reconstruction. Initialize the object and the pupil function. The related code is provided in lines 34–39 and 105–110 in Supplementary Software 'FP_simulationRecover.m'.

▲**CRITICAL STEP** For object initialization, we average all captured images to obtain an incoherent image and up-sample it to the same size as that of the reconstruction. The initial pupil function is defined as a circular aperture as in equation (8). The weights for Zernike modes are set to zeros.

49 Recover the pupil aberration. The related code is provided in lines 112–180 in Supplementary Software 'FP_simulationRecover.m'. The 'methodType' in the code is set as 'GD' for the recovery process. Refer to the section 'Software implementation of FP'.

50 Check whether the reconstruction quality of the object is comparable to the typical results. The left panel of Fig. 6 shows the typical recovered images of blood cells.

51 Save the recovered pupil as a .mat file.

■**PAUSE POINT** Load the .mat file and set this pupil as the initial guess when performing subsequent FP reconstructions.

Image acquisition and reconstruction ● Timing 0.5–1 h

▲**CRITICAL** Different from the previous pupil calibration section, we aim to shorten the acquisition time in a regular FP experiment. We take two approaches as follows. First, we set the camera's digital gain to 26 dB for darkfield image acquisition. As such, we can substantially shorten the acquisition time (originally 1 s now becomes 0.05 s). Second, we skip some of the LED elements that have high-illumination NAs (corresponding to darkfield images). Nonuniform sampling according to the illumination NAs is an effective strategy for reducing the number of acquisitions[76,84]. For all selected LED elements, we capture three sets of images of the same object with different camera gains and exposures. These three sets of images are then combined into one HDR dataset. We also note that multiple LED elements can be turned on at the same time to shorten the acquisition time[81,85,86]. The captured image can be modeled as an incoherent mixture of different coherent states[29,30].

52 Select a portion of the LED elements for the image acquisition process.

▲**CRITICAL STEP** As most signal energy concentrates in the central region of the Fourier spectrum, a higher density of sampling points can be adopted for the central region of the Fourier space. For dark-field images with large incident angles, the aperture overlap between adjacent acquisitions can be reduced. To this end, we keep all brightfield LEDs while skipping every other darkfield LED in the acquisition process.

53 Place the specimen under testing on the sample stage. Turn on the central LED of the illuminator. Open the IC Capture software. Adjust the focus knob to bring the image into focus. Close the IC Capture software.

54 Adjust the exposure time as in Step 38. This exposure time is set as the reference exposure.

55 Set different camera gains for the acquisition process. For each LED, we capture three images by setting the gain to 0, 26 and 26 dB, respectively (a gain of 26 dB amplifies the signals by 20 times).

? TROUBLESHOOTING

56 Turn on the selected LEDs sequentially. For the three sets of images, the exposure times are set to be 1-, 1- and 3.5-fold of the reference exposure time in Step 54. The total acquisition time is ~45 s. The

related code is provided in lines 91–137 in Supplementary Software 'FP_imageAcquisition.m' (under the 'experiment' mode).

▲**CRITICAL STEP** We note that we do not need to capture all three sets of images for some of the LEDs. For example, the second and the third sets of images will be overexposed under brightfield illumination. Similarly, the first set of images will be underexposed under darkfield illumination. Excluding these over- and underexposed images can further reduce the acquisition time.

57 Perform HDR combination of the captured three sets of images as in Step 47.

? TROUBLESHOOTING

58 Recover the object and update the pupil as in Steps 48–49.

▲**CRITICAL STEP** In this refinement step, the pupil is initialized as the prerecovered pupil in Step 49. The 'methodType' in the code is set as 'rPIE' for the refinement process.

? TROUBLESHOOTING

59 Check whether the image quality is comparable to the typical results. The left panel of Fig. 6 shows the recovered images of blood cells.

60 Save the results and close MATLAB.

Procedure 2: spatial-domain CP

Prepare the blood-coated sensor ● Timing 1 h

▲**CRITICAL** In the CP setup, a dense monolayer of blood cells severs as a high-performance computational bio-lens for the ptychographic reconstruction process. We recommend using goat blood for its low cost (US$29 per 50 ml) and the smallest cell size (2–3 µm) among all animals.

▲**CRITICAL** The goat blood can be smeared on the image sensor and then fixated with methanol (Steps 2–3). Alternatively, it can be smeared on a thin coverslip (Thorlabs, CG00C2) followed by methanol fixation. This blood-coated coverslip can then be attached to the image sensor, with the blood cells sandwiched in between the coverslip and the sensor's coverglass (Steps 4–8). For both options, blood fixation is critical to preserve cell morphology over a long period.

1 Take 1 ml of goat blood (Lampire, 7202501) with a pipette and put it into a centrifuge tube. Centrifuge the tube at 1,500 rpm for 5 min to separate the blood cells from the plasma. Alternatively, leave the tube in the refrigerator at 4 °C for 1 d. Blood cells can be separated from plasma by gravity.

2 Option 1: smear blood on the image sensor (Steps 2–3). Use a pipette to transfer 2 µl blood cells to one end of the image sensor (The Imaging Source, DMM 37UX226-ML). Position a glass slide at an angle of 30–45° to the image sensor. Drag the slide backward carefully to smear the blood over the image sensor, as shown in Fig. 7b.

▲**CRITICAL STEP** If the blood-cell layer is too thin or too thick, use alcohol and tissue paper to remove the layer and repeat the smearing process. An ideal coded surface contains a dense and uniform monolayer of blood cells covering the entire image sensor. Figure 3i shows a sample image of the blood-cell layer profile.

? TROUBLESHOOTING

3 Air dry the blood-cell layer and fixate it with methanol for 2 min.

4 Option 2: smear blood on a coverslip (Steps 4–8). Use a pipette to transfer 2 µl of goat blood on one end of a thin coverslip (Thorlabs, CG00C2).

5 Use a clean glass slide positioned at an angle of 30–45° to the coverslip. Drag the slide backward carefully to smear the blood over the entire coverslip, as shown in Fig. 7c.

6 Air dry the blood-cell layer and fix it with methanol for 2 min.

7 Prepare 2 ml silicone (Dow, SYLGARD 184 silicone elastomer kit) following a 10 (base) to 1 (curing agent) mixing ratio.

▲**CRITICAL STEP** If needed, use a vacuum desiccator (Amazon, SP Bel-Art 420200000) to remove the air bubbles in the mixed liquid.

8 Use a pipette to transfer 2 µl silicone liquid to the center of the image sensor. For the blood-coated coverslip, use a microscope to select a 7 × 7 mm region with a dense monolayer of blood cells. If such a region cannot be found, repeat Steps 4–6. Align this region with the image sensor. Attach the coverslip to the image sensor with the blood-cell layer and silicone liquid sandwiched in between. Press the coverslip to the image sensor and hold it for 1 d until they stick firmly with each other.

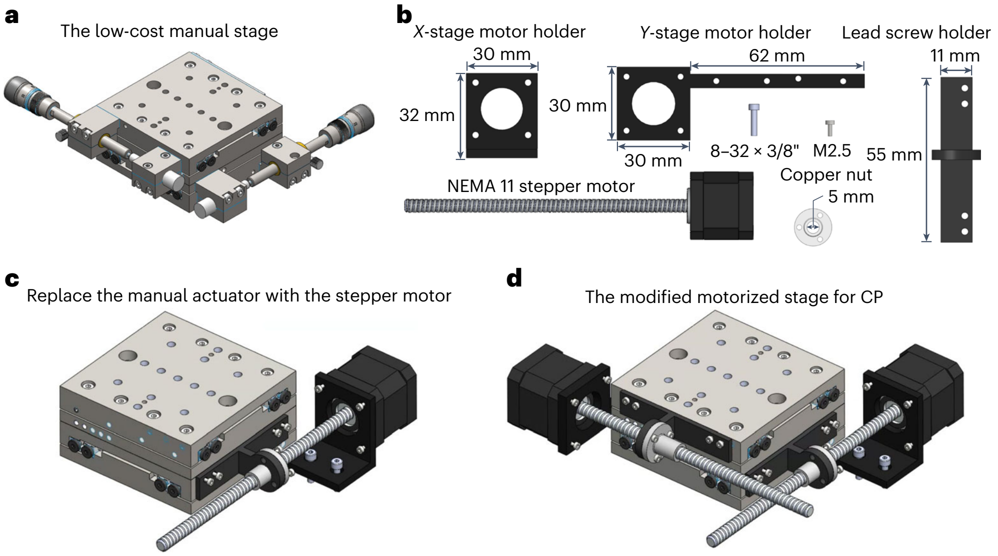

Fig. 10 | Stage assembling process for CP. a, The original low-cost manual stage. **b**, Different parts for stage modification. **c**, Replace the actuator with a stepper motor. **d**, The modified motorized stage.

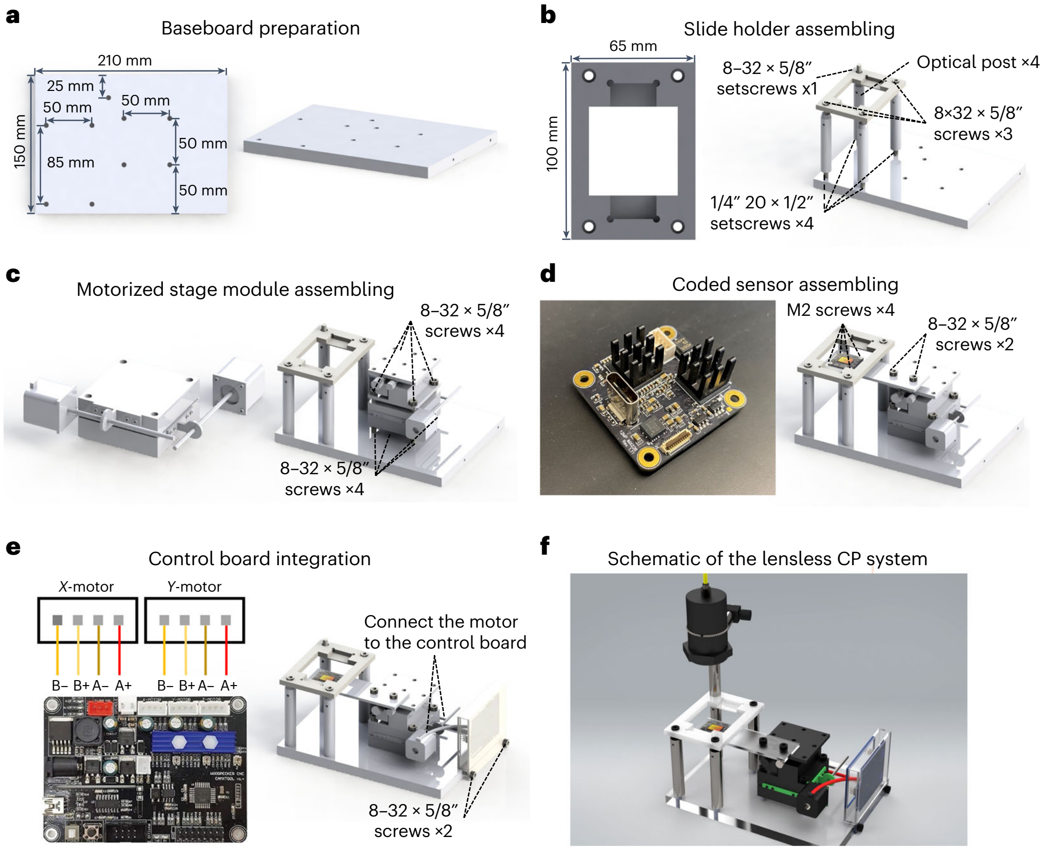

Fig. 11 | System integration for CP. a, Baseboard preparation. **b**, Slide holder assembling. **c**, Motorized stage assembling. **d**, Coded sensor assembling. **e**, Control board integration. **f**, A schematic of the CP system.

Motorized stage development and system integration ● Timing 1 d

▲CRITICAL We modify a compact *XYZ* three-axis manual stage for translating the blood-coated image sensor in the lateral directions. Figure 10 shows the overall stage assembling process, where we replace the manual actuators with stepper motors for motorized control. Figure 11 shows the assembling process of the CP platform, where we integrate the baseboard (Fig. 11a), the slide holder (Fig. 11b), the motorized stage (Fig. 11c), the coded sensor (Fig. 11d) and the control board (Fig. 11e) into a compact system (Fig. 11f).

▲CRITICAL In general, we do not need to collimate the laser light from the single-mode fiber for sample illumination (Step 18). However, the image quality of reconstruction may be degraded if the fiber is placed too close to the sample (<10 cm). If needed, one can collimate the laser light using a lens (Steps 19–20). A key consideration is to generate a large, collimated beam so that the intensity is uniform across the entire image sensor.

9 Attach two heat sinks (Alpha, LPD40-3B) to the integrated circuit chips of the image sensor board, as shown in Fig. 11d.

10 Mount the 405 nm fiber-coupled laser (Thorlabs, LP405-SF10) using the laser diode mount (Thorlabs, LDM9LP) and connect the laser with the driver (Thorlabs, ITC4001).

▲CRITICAL STEP We need only <5 mW output laser power and the corresponding exposure time is in the submillisecond range. The temperature controlling module is optional for the laser diode module.

11 Prepare the 3D-printed parts for building the motorized stage. The related SolidWorks design files are provided in Supplementary Data 'CP_stageSolidWorks.zip'. Assemble the motorized stage according to Fig. 10. Another option is to use a commercially available motorized stage for translating the blood-coated sensor.

12 Prepare the acrylic base with holes using the drilling machine (Delta, 12 drill press). Figure 11a shows the design of the acrylic base. The SolidWorks design file is provided in Supplementary Data 'CP_base.SLDPRT'.

13 Make a sample holder using the milling machine (Roland, monoFab SRM-20). Attach the sample holder to the acrylic base using four optical posts (Thorlabs, TR3). Figure 11b shows the dimension of the sample holder and the detailed assembling process. The SolidWorks design file is provided in Supplementary Data 'CP_sampleHolder.SLDPRT'.

14 Attach the motorized stage from Step 11 to the acrylic base, as shown in Fig. 11c.

15 Make a sensor holder using the milling machine. Assemble the blood-coated sensor onto the sensor holder. Attach the sensor holder onto the motorized stage using screws, as shown in Fig. 11d. The SolidWorks design file is provided in Supplementary Data 'CP_sensorHolder.SLDPRT'.

16 Place the GRBL three-axis control board (Amazon, ASIN: B083BFBBVY) at the side of the acrylic base. Connect the wires from the motorized stage to the control board, as shown in Fig. 11e. The SolidWorks design files are provided in Supplementary Data 'CP_motorHolderSolidWorks.zip'.

17 Attach an optical post (Thorlabs, TR4) to the corner of the slide holder.

18 Option 1: noncollimated beam from the fiber (Step 18). Attach a 1 inch tube slip ring (Thorlabs, SM1RC) to the post on the slide holder. Attach a fiber adaptor (Thorlabs, S120-FC) to an optical tube (Thorlabs, SM1L20) and mount the assembly to the tube slip ring. Adjust the axial position of the assembly. Connect the single-mode fiber to the fiber adaptor, as shown in Fig. 11f.

▲CRITICAL STEP In the calibration process, the illumination beam information is coded into the blood-cell layer profile on the image sensor. Therefore, we can simply model the spherical wave from the fiber as a plane wave for both the calibration and the subsequent CP experiments. However, if the fiber source is placed too close to the sample (<10 cm), this plane-wave approximation may fail, and the resulting image quality will be degraded. We recommend a distance of >15 cm between the fiber source and the coded sensor.

? TROUBLESHOOTING

19 Option 2: collimated beam (Steps 19–20). Connect the single-mode fiber to the fiber adaptor (Thorlabs, S120-FC). Turn on the laser. Collimate the fiber-coupled light source using a 2 inch, 200 mm bi-convex lens (Thorlabs, LB1199) mounted on an adjustable lens tube (Thorlabs, SM2V15). Turn off the laser after the collimation process.

! CAUTION Wear eye protection goggles when working with the laser. Proper laser safety training is also required.

20 Attach a 2 inch tube slip ring (Thorlabs, SM2RC) to the post on the slide holder. Attach the collimated light source to the tube slip ring. Adjust the axial position of the assembly. We recommend a distance of 5–10 cm between the collimated lens to the image sensor.

21 For both options, turn on the laser and align the beam so that the image sensor locates at the beam center. Turn off the laser after the alignment process.

Motion tracking based on the captured images ● Timing 0.5–1 h

▲ **CRITICAL** We estimate the positional shifts of the coded sensor via the iterative correlation analysis approach discussed in Box 2. Precise mechanical scanning is not required in our implementation.

22 Install MATLAB with the Image Acquisition Toolbox.

23 Install IC Capture and the driver for the 33U series (Version 5.1.0.1719) of the image sensor (The Imaging Source, DMM 37UX226-ML).

24 Install CUDA driver (CUDA Toolkit v11.7) for the Nvidia graphics card.

25 Install the driver for GRBL motor control board. The driver is provided in Supplementary Software 'CP_CH340SER.EXE'.

26 Connect the motor control board to the computer. Connect the control board with a 24 V/2 A power source.

27 Connect the image sensor to the computer using a USB 3.0 type C cable. Open MATLAB, initialize the parameters of the image sensor. The related code is provided in lines 15–24 in Supplementary Software 'CP_image AcquisitionCalibration.m'.

28 Use a stained blood smear slide (Carolina, 313158) as a calibration object. Attach this slide to the sample holder (with the blood cells and the coverslip facing the coded sensor). Adjust the axial position of the coded sensor using the *Z* stage. We recommend a small distance of <0.5 mm between the object and the coded surface.

▲ **CRITICAL STEP** The blood smear slide is an ideal calibration object as it contains fine spatial features over the entire microscope slide.

29 Turn on the laser. Adjust the exposure time of the image sensor. The related code is provided in lines 26–33 in Supplementary Software 'CP_imageAcquisitionCalibration.m'. The ratio of overexposed pixels should be kept <0.01%.

▲ **CRITICAL STEP** A proper exposure time is needed to avoid capturing severely overexposed raw images. A darkroom is also recommended to reduce the signals generated by ambient light.

? TROUBLESHOOTING

30 Turn on the stage motor and initialize the stage scanning parameters. The related code is provided in lines 35–45 in Supplementary Software 'CP_imageAcquisitionCalibration.m'.

31 Capture 1,500 raw images by translating the sensor in a spiral route. The related code is provided in lines 66–91 in Supplementary Software 'CP_imageAcquisitionCalibration.m'. We recommend a step size of 1–2 μm in the scanning process.

32 Turn off the laser and save the captured raw images.

33 Convert the captured image format to 'single' and crop a subregion for each image. Generate the initial reference image 'imRefInitial'. Estimate the subpixel shifts by locating the maximum point of the cross-correlation maps between the reference image and all cropped tiles (Supplementary Fig. 3a). The related code is provided in lines 125–126 in Supplementary Software 'CP_simulationRecover.m', where the function 'dftregistration' is used for cross-correlation analysis[83] (for the discussion, also refer to Box 2).

? TROUBLESHOOTING

34 Shift back the cropped tiles on the basis of the estimated shifts and generate the refined reference image 'imRefRefine'. Refine the translational shifts via a cross-correlation analysis between the reference image and all cropped tiles. The related code is provided in lines 127–130 in Supplementary Software 'CP_simulationRecover.m'.

35 Repeat Step 34 until the estimated route converges (Supplementary Fig. 3b).

? TROUBLESHOOTING

Recover the coded surface profile ● Timing 1–2 h

▲ **CRITICAL** We use the calibration blood smear slide to recover the coded surface profile on the image sensor.

▲CRITICAL We recommend using a graphics processing unit with at least 24 GB of memory for the reconstruction process. One can either recover the full field of view of the sensor or crop a smaller region for testing. We note that the size of the cropped region is recommended to be at least 1,024 × 1,024 pixels. A small cropped region can lead to degradation of the spatial resolution.

36 Shift back and average all measurements. Initialize the object wavefront 'objectIniGuess'. The related code is provided in lines 134–144 in Supplementary Software 'CP_simulationRecover.m'.
▲CRITICAL STEP We recommend using at least three-fold up-sampling for achieving a good spatial resolution.

37 Initialize the coded surface profile 'CSIniGuess'. The related code is provided in lines 146–147 in Supplementary Software 'CP_simulationRecover.m'.

38 Perform iterative ptychographic reconstruction. The related code is provided in lines 161–209 in Supplementary Software 'CP_simulationRecover.m'.
▲CRITICAL STEP The parameters 'alphaO' and 'alphaS' in the rPIE algorithm are set to '1' in our implementation for simplicity.

39 Check the quality of the recovered coded surface. The sample image of the coded surface can be found in Fig. 3i. Save the calibrated coded surface profile as a .mat file.
■PAUSE POINT The saved .mat file can be used for the subsequent experiments. Load this file when imaging other specimens.

? TROUBLESHOOTING

Image acquisition and reconstruction ● Timing 1–2 h

▲CRITICAL In this section, we perform image acquisition and reconstruction using the prerecovered coded layer profile. The images are captured when the sample is in continuous motion. The acquisition time is ~12 s for ~300 raw measurements. The reconstruction process shares a similar workflow as in the previous section.

40 Attach the specimen under testing to the sample holder. Adjust the axial position of the coded sensor using the Z stage.
! CAUTION For live-cell imaging, we recommend covering the electronics with waterproof coating.

41 Turn on the laser. Modify the scanning parameters. The related code is provided in lines 40–45 in Supplementary Software 'CP_imageAcquisitionExperiment.m'. The targeted scanning step size is 1–2 µm between adjacent measurements.

42 Acquire 300 images at a framerate of 30 fps. The related code is provided in lines 53–93 in Supplementary Software 'CP_imageAcquisitionExperiment.m'. The total acquisition time is ~12 s.

43 Repeat Steps 40 and 42 for additional sample acquisitions, if needed. Repeat Step 42 for time-lapse monitoring. Turn off the laser after the image acquisition process.

44 Refer to Steps 33–35 to estimate the positional shifts from the captured raw images. Supplementary Fig. 3b shows the estimated scanning route of the coded sensor.
▲CRITICAL STEP Avoid selecting a region with few objects for positional tracking. Otherwise, the estimated positional shifts may be inaccurate.
? TROUBLESHOOTING

45 Load the prerecovered coded surface profile. Initialize the object wavefront as in Step 36.

46 Perform iterative reconstruction as in Step 38.
▲CRITICAL STEP We typically use five iterations for image reconstruction. For the first three to four iterations, we only update the object exit wavefront, and for the last one to two iterations, we can jointly update both the object and the coded surface profile for refinement.
▲CRITICAL STEP For live-cell imaging experiments, the temporal correlation between adjacent timepoints can be adopted as an additional constraint for the reconstruction process. One can use the recovered object exit wavefront at the previous timepoint as the initial guess for the current timepoint.
? TROUBLESHOOTING

47 Digitally propagate the recovered object exit wavefront back to the object plane.

48 Check whether the image quality is comparable to the typical results. The left panel of Fig. 9 shows the recovered images of blood cells.

49 Save the results as a .mat file and close MATLAB.

Troubleshooting

For FP imaging, we summarize the representative problems in Fig. 12. The typical raw FP measurements of a blood smear slide are shown in Fig. 12a and the corresponding FP recovered images are shown in Fig. 12b. In comparison, Fig. 12c–k shows FP reconstructions with different underlying problems. For lensless CP imaging, we summarize the representative problems in Fig. 13. The raw image and the correct CP reconstruction are shown in Fig. 13a. In comparison, Fig. 13b–f shows the raw images and their CP reconstructions with different underlying problems. Table 1 discusses the causes of these imaging problems in both systems. It also provides corresponding troubleshooting advice.

We note that, for both FP and CP, it is important to obtain the ptychographic probe from calibration experiments. Figure 14 shows the reconstructions with and without using the pre-calibrated ptychographic probes. With FP, the solution often falls to a local minimum with a large and unknown pupil aberration. With CP, the slow-varying object phase often results in solution ambiguities when the coded surface is unknown in the reconstruction process.

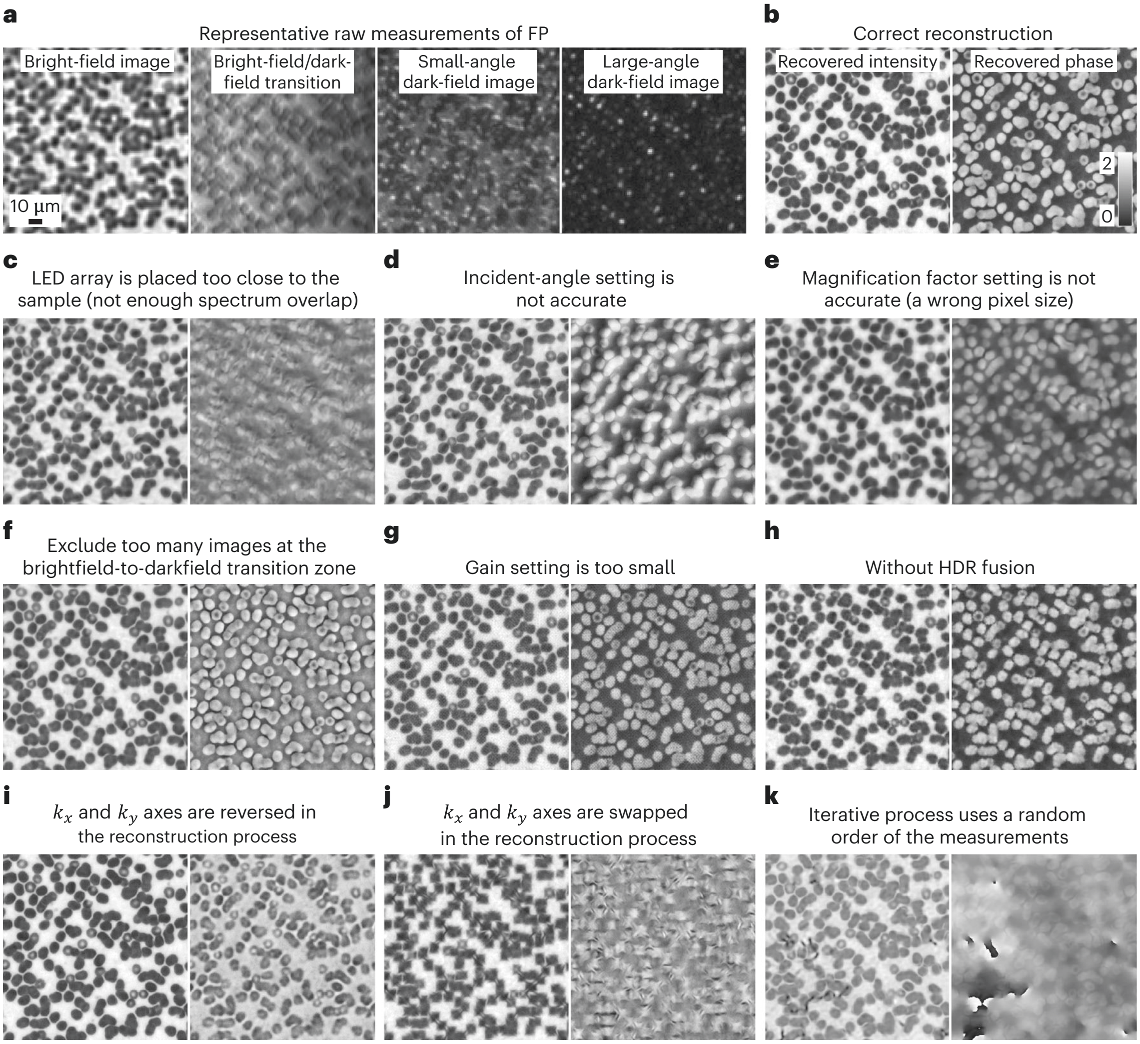

Fig. 12 | Troubleshooting for FP. **a**, Representative raw measurements for FP. **b**, The correct FP reconstruction. **c**–**k**, The FP reconstructions with different underlying problems in the reconstruction process.

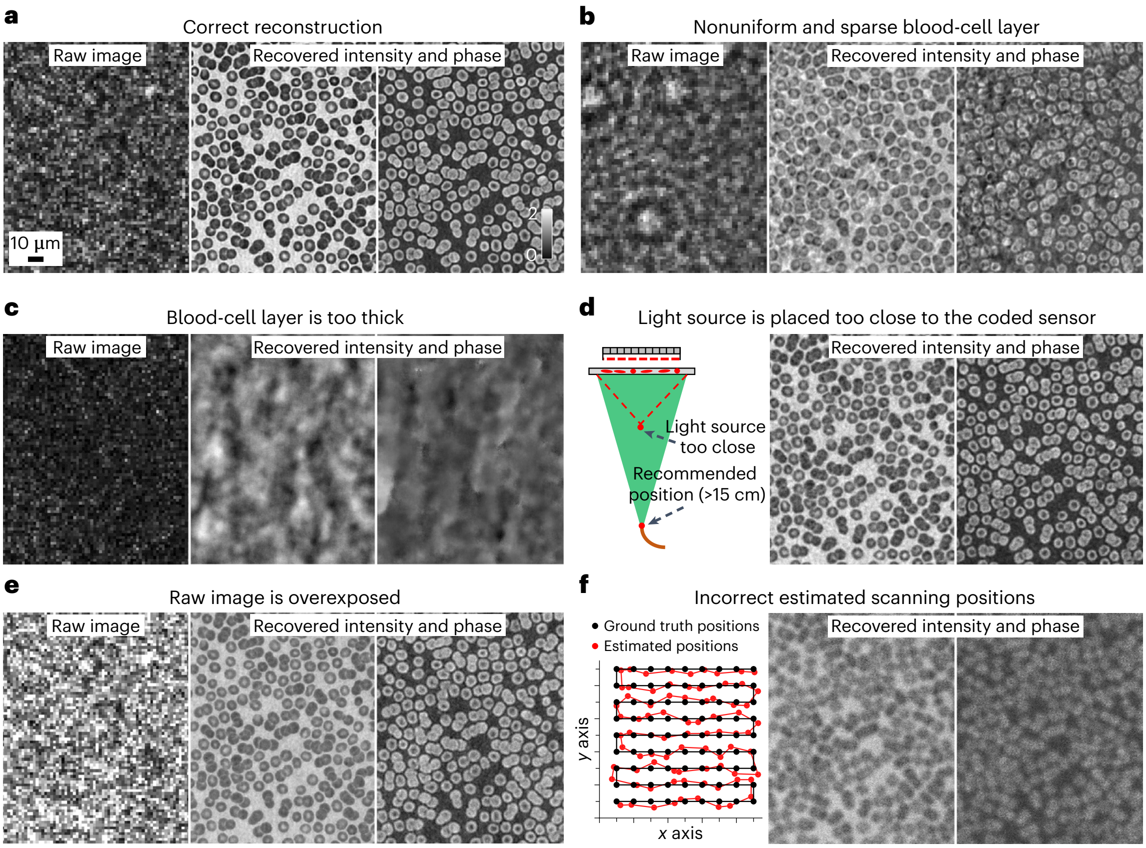

Fig. 13 | Troubleshooting for CP. a, The correct CP reconstruction. **b–f**, CP reconstructions with different underlying problems.

Table 1 | Troubleshooting table for FP and CP

Step	Problem	Possible reason	Solution
Procedure 1, Step 15	Poor quality for the recovered phase in Fig. 12c	The LED array is placed too close to the sample, resulting in insufficient spectrum overlapping in the Fourier space	Increase the distance between the sample stage and the illuminator
Procedure 1, Step 21	The recovered phase exhibits shadow effects in Fig. 12d	The incident wavevectors of different LED elements are not accurate	Recalibrate the incident wavevectors for the reconstruction process
Procedure 1, Step 32	Degraded reconstruction quality in Fig. 12e	The magnification factor of the system has not been calibrated	Follow Procedure 1, Steps 29–32 to calibrate the magnification factor of the objective lens and obtain the correct detector pixel size at the object plane
Procedure 1, Step 47	As shown in Fig. 12f, the recovered phase has low contrast and the background of the phase is not uniform	Exclude too many images at the brightfield-to-darkfield transition zone	When the illumination NA is close to the objective NA, the captured image contains low-frequency phase information that is critical for phase recovery[60]. Instead of excluding the entire image in Procedure 1, Step 47, we can generate a binary mask to only exclude the pixels in the brightfield-to-darkfield transition zone[15,87]. Similarly, we can exclude pixels exposed to the system stray light (refer to Supplementary Fig. 4)
Procedure 1, Step 55	Noisy reconstruction as shown in Fig. 12g	Camera gain is too small	Set a larger camera gain or increase the exposure time
Procedure 1, Step 57	Degraded image quality as shown in Fig. 12h	Without performing the HDR combination	Capture three sets of images with different camera gains and exposures. Perform HDR combination in Procedure 1, Step 47
Procedure 1, Step 58	As shown in Fig. 12i, the recovered phase has a higher value in the background than that in the feature region	The k_x and k_y axes are reversed in the reconstruction process	Reverse the k_x and k_y axes
Procedure 1, Step 58	As shown in Fig. 12j, square artifacts are presented in the reconstruction	The k_x and k_y axes are swapped and/or reversed in the reconstruction process	Swap and/or reverse the k_x and k_y axes
Procedure 1, Step 58	Artifacts are presented in the recovered images, as shown in Fig. 12k	The iterative process uses a random order of the measurements	Use a recovery sequence ranked by the illumination NAs of the LED elements[76]

Table continued

Table 1 (continued)

Step	Problem	Possible reason	Solution
Procedure 1, Step 58	Degraded reconstruction quality at the edge of the field of view, as shown in Fig. 14c	The pupil is not correctly initialized from the calibration experiment	Repeat the calibration experiment. Properly initialize the pupil aberration
Procedure 2, Step 2	Degraded reconstruction quality as shown in Fig. 13b	The blood-cell layer is nonuniform and sparse	Use alcohol and tissue paper to remove the blood-cell layer on the sensor. Repeat the smearing process as in Procedure 2, Step 2
Procedure 2, Step 2	Fail to recover the images as shown in Fig. 13c	The blood-cell layer is too thick in certain regions	Use alcohol and tissue paper to remove the blood-cell layer on the sensor. Repeat the smearing process as in Procedure 2, Step 2
Procedure 2, Step 18	Degraded reconstruction quality as shown in Fig. 13d	The laser fiber is placed too close to the sample	Place the fiber head at least 15 cm away from the coded sensor
Procedure 2, Step 29	The raw image has too many overexposed pixels, as shown in Fig. 13e	The exposure time is not properly set, or the output power of the laser fluctuates over time	Adjust the exposure time as in Procedure 2, Step 29. Check the mean intensity of different captured images. If it changes noticeably between different measurements, check the drive current and the temperature of the laser diode
Procedure 2, Step 29	The contrast of the raw images is low with a strong background	The ambient light creates an incoherent background on the captured images	Perform the experiment in a dark environment
Procedure 2, Step 33	The estimated positions are all zeros	The blood-cell layer is too thick	Use alcohol and tissue paper to remove the blood-cell layer on the sensor. Repeat the smearing process as in Procedure 2, Step 2
Procedure 2, Step 35	The estimated scanning route is different from the preset spiral route in the calibration process	The estimated positions are inaccurate	Repeat Procedure 2, Step 34 to further refine the estimated route
Procedure 2, Step 39	The recovered coded surface profile is defocused and blurry	The distance between the coded surface and the pixel array is not properly set	Digitally propagate the blood-coated surface profile to different z positions. Select one with the best performance and set it as the 'd_2' (in Fig. 2). Repeat the calibration process in Procedure 2, Steps 36–38
Procedure 2, Step 44	The estimated scanning route deviates considerably from the preset route, as shown in Fig. 13f	The estimated positions are inaccurate	Repeat Procedure 2, Step 34 to further refine the estimated route. If the problem still exists, select another region for motion tracking
Procedure 2, Step 46	The phase wraps cannot be properly recovered, as shown in Fig. 14d	The coded surface profile is jointly updated with the object in the reconstruction process	Do not update the coded surface profile in the reconstruction process

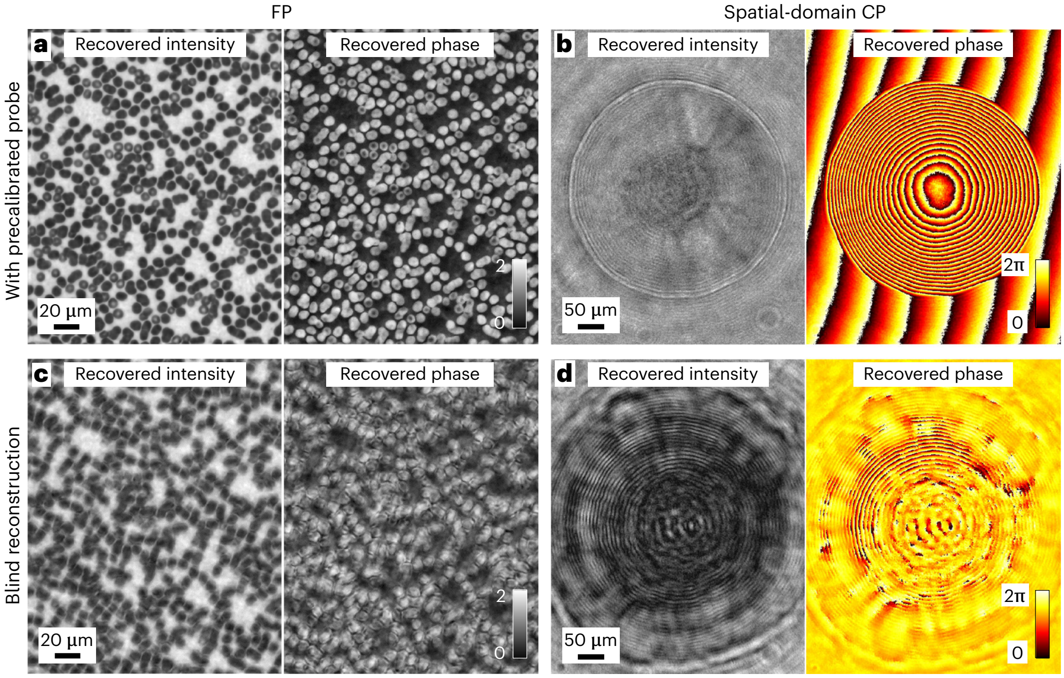

Fig. 14 | Reconstructions with precalibrated ptychographic probes versus blind reconstructions. a, On the basis of the pupil aberration obtained from the calibration experiment, FP can correctly recover the blood cells located at the edge of the field of view. **b**, On the basis of the blood-cell layer obtained from the calibration experiment, CP can recover the slow-varying bacterial colony profile with many 2π wraps. **c**, For FP, blind ptychographic reconstructions fail to recover the blood cells located at the edge of the field of view. **d**, For CP, blind ptychographic reconstructions fail to correctly recover the slow-varying bacterial colony profile.

Timing

Procedure 1: FP

Steps 1–8, programable light source development: 3–5 h
Steps 9–27, system integration and alignment: 1–2 h
Steps 28–43, incident angle calibration: 0.5–1 h
Steps 44–51, recover the pupil aberration: 2–3 h
Steps 52–60, image acquisition and reconstruction: 0.5–1 h

Procedure 2: Spatial-domain CP

Steps 1–8, prepare the blood-coated surface: 1 h
Steps 9–21, motorized stage development and system integration: 1 d
Steps 22–35, motion tracking based on the captured images: 0.5–1 h
Steps 36–39, recover the coded surface profile: 1–2 h
Steps 40–49, image acquisition and reconstruction: 1–2 h

Anticipated results

Anticipated results for FP

The successful implementation of the protocol yields an FP system capable of imaging different biospecimens with high resolution and a large field of view. Figure 15a shows a recovered gigapixel image of a blood smear slide[36]. The insets of Fig. 15a show the aberration pupils of two different regions at the edge

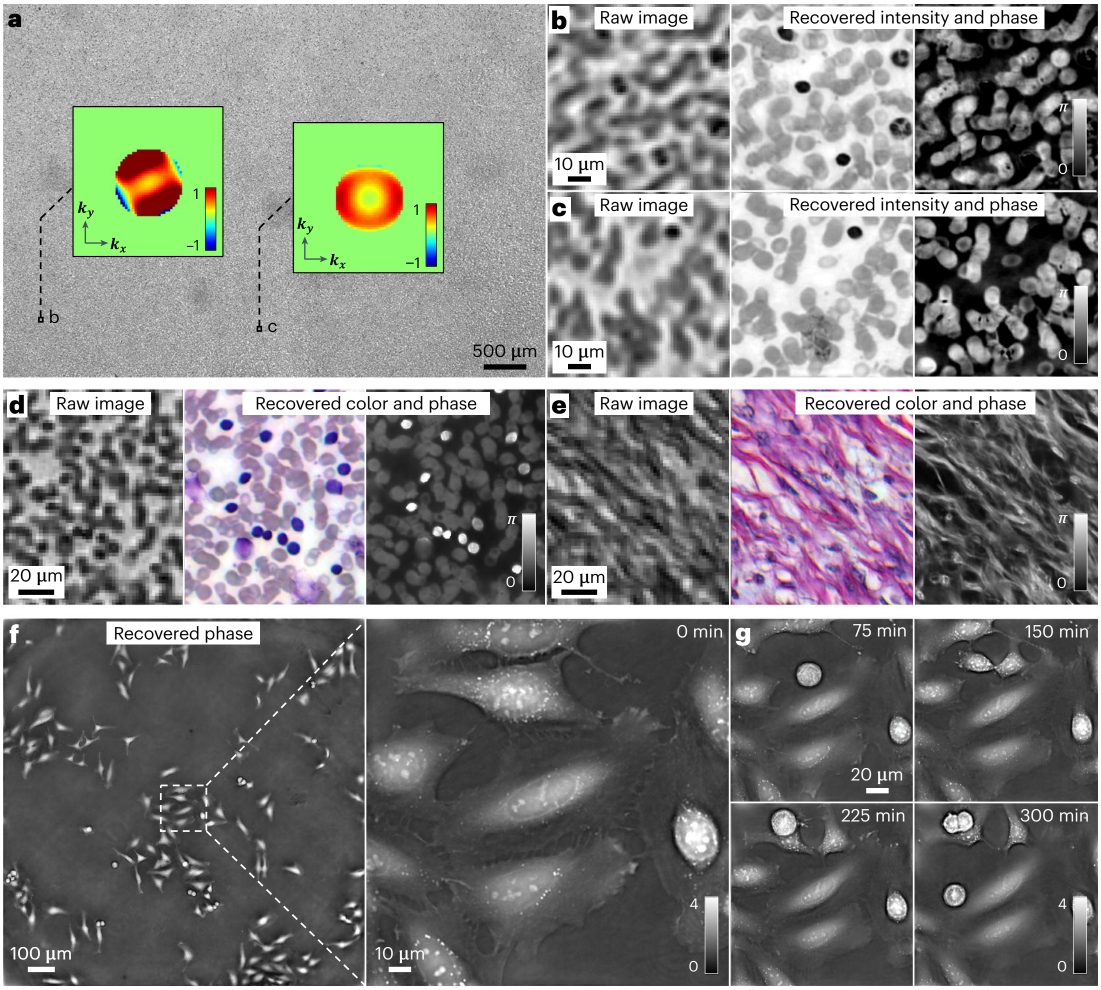

Fig. 15 | Representative imaging results using FP. a–**c**, The recovered gigapixel image of a blood smear slide (**a**) and its zoomed-in views (**b** and **c**). **d**,**e**, The recovered color and phase images of a blood smear slide (**d**) and a stained tissue section (**e**). **f**, The recovered phase image of HeLa cells on a Petri dish. **g**, Monitoring the cell culture growth in a longitudinal study. **a**–**c** adapted from ref. [36] under Creative Commons license CC BY 4.0; **d** and **e** from ref. [15], Springer Nature Ltd; and **f** and **g** from ref. [60], Springer Nature Ltd.

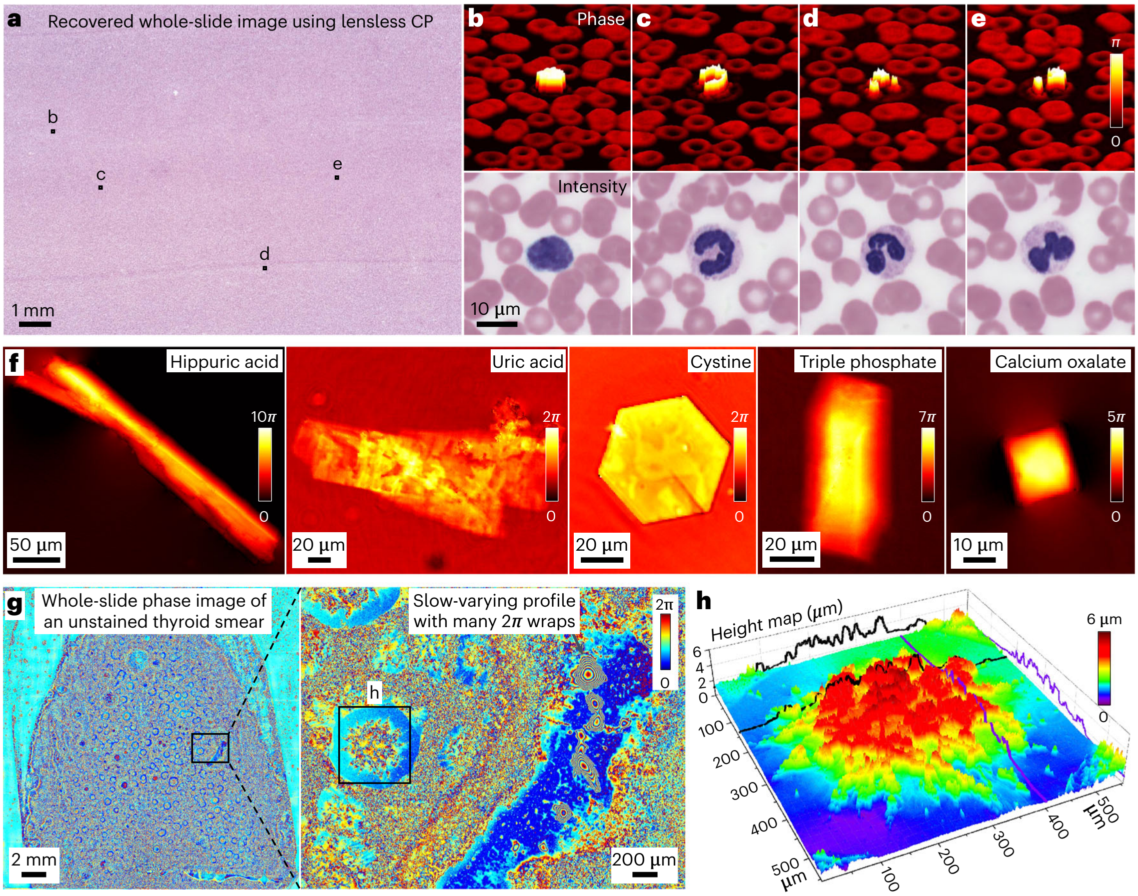

Fig. 16 | Imaging fixed biospecimens using CP. a, The recovered whole-slide image of a blood smear slide[11]. **b**–**e**, Zoomed-in views of the white blood cells in **a**. **f**, The recovered unwrapped phase images of different crystals in a urine sediment slide[13]. **g**, The recovered whole-slide phase image of an unstained thyroid smear[12]. **h**, The recovered height map of a zoomed-in region of **g**. **a**–**e** adapted with permission from ref. [11], American Chemical Society; **f** from ref. [13], American Chemical Society; and **g** and **h** from ref. [12], Royal Society of Chemistry.

of the field of view. These pupils are recovered by updating the weights of Zernike modes. Figure 15b,c shows the zoomed-in views of the recovered blood smear slide, where we can see notable resolution improvement from the raw images to the FP results. Since the employed LED illuminator contains red, green and blue LEDs, we can also perform sequential FP acquisitions under these wavelengths for color imaging. Figure 15d,e shows the raw images and the color FP reconstructions of stained blood smear and tissue section samples[15]. FP can also be used for label-free live-cell imaging over a long period. Figure 15f shows the recovered phase image of live human cervical adenocarcinoma epithelial (HeLa) cells on a Petri dish[60]. Cell mitosis and apoptosis events can be monitored in a time-lapse experiment in Fig. 15g.

Anticipated results for lensless CP

CP shares the same benefits with FP of large-field-of-view and high-resolution imaging. The lensless nature and its modulation strategy provide additional benefits for imaging thick biospecimens with nanometer sensitivity. Figure 16a shows the recovered whole slide image of a blood smear slide[11]. The zoomed-in views are shown in Fig. 16b–e, where we can clearly resolve the detailed structures of the white blood cells. Figure 16f shows the recovered images of different crystals of a urine sediment slide[13]. The phase profiles of these crystals before the unwrapping process contain many 2π wraps that are difficult to recover using other common phase retrieval approaches. Figure 16g shows the recovered whole slide phase image of an unstained thyroid smear[12] and Fig. 16h shows the recovered height map of a zoomed-in region.

In addition to imaging fixed biospecimens, we can also use CP to perform high-resolution live-cell monitoring over a large field of view. Figure 17a shows the recovered phase images of bacterial cells at different timepoints[14]. Figure 17b shows the 3D phase map of the microcolonies, where we can directly observe the forming of layered structures. In particular, the projected line traces in Fig. 17b show two-layer and three-layer structures, with ~0.5 radians of phase accumulation for each layer. The multilayer forming

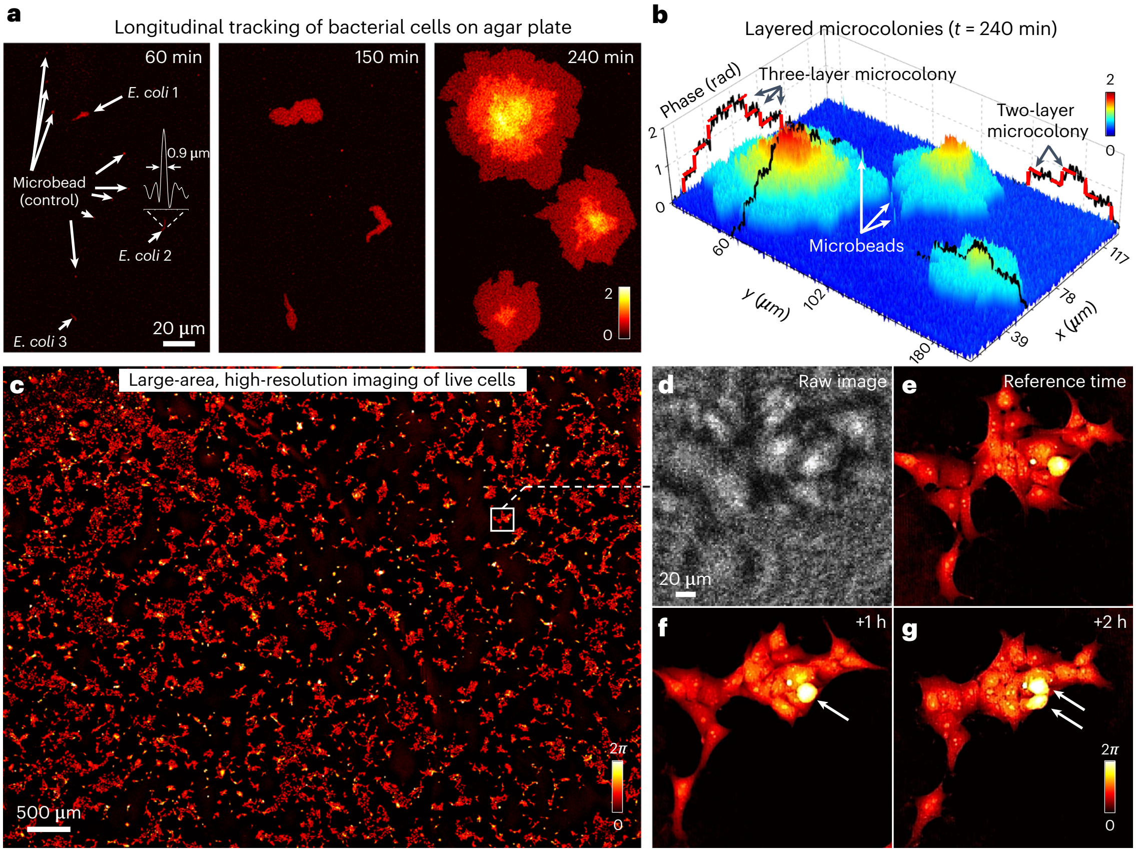

Fig. 17 | Time-lapse monitoring of live cells using lensless CP. **a**, The recovered phase images of bacterial cultures at different timepoints. **b**, The recovered phase map reveals the layered structure of 3D bacterial colonies. **c**, The recovered high-resolution phase image of live HEK 293 cells over a large field of view. **d**, The zoomed-in view of the captured raw image. **e**–**g**, The corresponding recovered phase images at different timepoints. **a** and **b** adapted with permission from ref. [14], Elsevier.

process occurs at the center while the monolayer remains in the outer regions. Figure 17c shows the recovered phase image of live human embryonic kidney 293 (HEK 293) cells over a large field of view. A zoomed-in view of the raw image is provided in Fig. 17d. The corresponding recovered phase images at different timepoints are shown in Fig. 17e–g, where we can clearly observe the cell proliferation process.

Reporting summary

Further information on research design is available in the Nature Portfolio Reporting Summary linked to this article.

Data availability

The main data supporting this study are available within the article, Supplementary Data and the primary supporting study[10,11,14]. Experimental datasets for both setups in this study are available in Zenodo: https://doi.org/10.5281/zenodo.7492626.

Code availability

All related MATLAB and Arduino code is provided in Supplementary Software. Additional code for testing experimental datasets is available in Zenodo: https://doi.org/10.5281/zenodo.7492626.

References

1. Sayre, D. Some implications of a theorem due to Shannon. *Acta Crystallogr.* **5**, 843–843 (1952).
2. Hoppe, W. Diffraction in inhomogeneous primary wave fields. 1. Principle of phase determination from electron diffraction interference. *Acta Crystallogr* **25**, 495–501 (1969).
3. Guizar-Sicairos, M. & Thibault, P. Ptychography: a solution to the phase problem. *Phys. Today* **74**, 42–48 (2021).

4. Faulkner, H. M. L. & Rodenburg, J. Movable aperture lensless transmission microscopy: a novel phase retrieval algorithm. *Phys. Rev. Lett.* **93**, 023903 (2004).
5. Rodenburg, J. & Maiden, A. in *Springer Handbook of Microscopy* 819–904 (Springer, 2019).
6. Wang, T. et al. Optical ptychography for biomedical imaging: recent progress and future directions. *Biomed. Opt. Express* **14**, 489–532 (2023).
7. Loetgering, L., Witte, S. & Rothhardt, J. Advances in laboratory-scale ptychography using high harmonic sources. *Opt. Express* **30**, 4133–4164 (2022).
8. Pfeiffer, F. X-ray ptychography. *Nat. Photonics* **12**, 9–17 (2018).
9. Jiang, Y. et al. Electron ptychography of 2D materials to deep sub-ångström resolution. *Nature* **559**, 343–349 (2018).
10. Zheng, G., Horstmeyer, R. & Yang, C. Wide-field, high-resolution Fourier ptychographic microscopy. *Nat. Photonics* **7**, 739 (2013).
11. Jiang, S. et al. Resolution-enhanced parallel coded ptychography for high-throughput optical imaging. *ACS Photonics* **8**, 3261–3271 (2021).
12. Jiang, S. et al. High-throughput digital pathology via a handheld, multiplexed, and AI-powered ptychographic whole slide scanner. *Lab Chip* **22**, 2657–2670 (2022).
13. Jiang, S. et al. Blood-coated sensor for high-throughput ptychographic cytometry on a Blu-ray disc. *ACS Sens.* **7**, 1058–1067 (2022).
14. Jiang, S. et al. Ptychographic sensor for large-scale lensless microbial monitoring with high spatiotemporal resolution. *Biosens. Bioelectron.* **196**, 113699 (2022).
15. Zheng, G., Shen, C., Jiang, S., Song, P. & Yang, C. Concept, implementations and applications of Fourier ptychography. *Nat. Rev. Phys.* **3**, 207–223 (2021).
16. Pan, A., Zuo, C. & Yao, B. High-resolution and large field-of-view Fourier ptychographic microscopy and its applications in biomedicine. *Rep. Prog. Phys.* **83**, 096101 (2020).
17. Konda, P. C. et al. Fourier ptychography: current applications and future promises. *Opt. Express* **28**, 9603–9630 (2020).
18. Guo, K., Dong, S. & Zheng, G. Fourier ptychography for brightfield, phase, darkfield, reflective, multi-slice, and fluorescence imaging. *IEEE J. Sel. Top. Quantum Electron.* **22**, 77–88 (2015).
19. Horstmeyer, R., Chung, J., Ou, X., Zheng, G. & Yang, C. Diffraction tomography with Fourier ptychography. *Optica* **3**, 827–835 (2016).
20. Zuo, C., Sun, J., Li, J., Asundi, A. & Chen, Q. Wide-field high-resolution 3D microscopy with Fourier ptychographic diffraction tomography. *Opt. Lasers Eng.* **128**, 106003 (2020).
21. Dong, S. et al. Aperture-scanning Fourier ptychography for 3D refocusing and super-resolution macroscopic imaging. *Opt. Express* **22**, 13586–13599 (2014).
22. Holloway, J., Wu, Y., Sharma, M. K., Cossairt, O. & Veeraraghavan, A. SAVI: synthetic apertures for long-range, subdiffraction-limited visible imaging using Fourier ptychography. *Sci. Adv.* **3**, e1602564 (2017).
23. Zhang, H. et al. Near-field Fourier ptychography: super-resolution phase retrieval via speckle illumination. *Opt. Express* **27**, 7498–7512 (2019).
24. Xiang, M. et al. Coherent synthetic aperture imaging for visible remote sensing via reflective Fourier ptychography. *Opt. Lett.* **46**, 29–32 (2021).
25. Wakonig, K. et al. X-ray Fourier ptychography. *Sci. Adv.* **5**, eaav0282 (2019).
26. Zhang, F., Pedrini, G. & Osten, W. Phase retrieval of arbitrary complex-valued fields through aperture-plane modulation. *Phys. Rev. A* **75**, 043805 (2007).
27. Maiden, A. M., Rodenburg, J. M. & Humphry, M. J. Optical ptychography: a practical implementation with useful resolution. *Opt. Lett.* **35**, 2585–2587 (2010).
28. Song, P. et al. Super-resolution microscopy via ptychographic structured modulation of a diffuser. *Opt. Lett.* **44**, 3645–3648 (2019).
29. Thibault, P. & Menzel, A. Reconstructing state mixtures from diffraction measurements. *Nature* **494**, 68–71 (2013).
30. Batey, D. J., Claus, D. & Rodenburg, J. M. Information multiplexing in ptychography. *Ultramicroscopy* **138**, 13–21 (2014).
31. Song, P. et al. Super-resolved multispectral lensless microscopy via angle-tilted, wavelength-multiplexed ptychographic modulation. *Opt. Lett.* **45**, 3486–3489 (2020).
32. Thibault, P., Dierolf, M., Bunk, O., Menzel, A. & Pfeiffer, F. Probe retrieval in ptychographic coherent diffractive imaging. *Ultramicroscopy* **109**, 338–343 (2009).
33. Guizar-Sicairos, M. & Fienup, J. R. Phase retrieval with transverse translation diversity: a nonlinear optimization approach. *Opt. Express* **16**, 7264–7278 (2008).
34. Maiden, A. M. & Rodenburg, J. M. An improved ptychographical phase retrieval algorithm for diffractive imaging. *Ultramicroscopy* **109**, 1256–1262 (2009).
35. Ou, X., Zheng, G. & Yang, C. Embedded pupil function recovery for Fourier ptychographic microscopy. *Opt. Express* **22**, 4960–4972 (2014).
36. Song, P. et al. Full-field Fourier ptychography (FFP): spatially varying pupil modeling and its application for rapid field-dependent aberration metrology. *APL Photonics* **4**, 050802 (2019).
37. Gustafsson, M. G. Surpassing the lateral resolution limit by a factor of two using structured illumination microscopy. *J. Microsc.* **198**, 82–87 (2000).
38. Liang, M. & Yang, C. Implementation of free-space Fourier ptychography with near maximum system numerical aperture. *Opt. Express* **30**, 20321–20332 (2022).

39. Schiske, P. Image reconstruction by means of focus series. In *Proc. 4th European Conference on Electron Microscopy, Rome, Italy* (Tipografia poliglotta, 1968).
40. Bao, P., Zhang, F., Pedrini, G. & Osten, W. Phase retrieval using multiple illumination wavelengths. *Opt. Lett.* **33**, 309–311 (2008).
41. Greenbaum, A. & Ozcan, A. Maskless imaging of dense samples using pixel super-resolution based multi-height lensfree on-chip microscopy. *Opt. Express* **20**, 3129–3143 (2012).
42. Luo, W., Zhang, Y., Feizi, A., Göröcs, Z. & Ozcan, A. Pixel super-resolution using wavelength scanning. *Light Sci. Appl.* **5**, e16060–e16060 (2016).
43. Zuo, C. et al. Transport of intensity equation: a tutorial. *Opt. Lasers Eng.* **135**, 106187 (2020).
44. Fienup, J. R. Phase retrieval algorithms: a comparison. *Appl. Opt.* **21**, 2758–2769 (1982).
45. Bishara, W., Su, T.-W., Coskun, A. F. & Ozcan, A. Lensfree on-chip microscopy over a wide field-of-view using pixel super-resolution. *Opt. Express* **18**, 11181–11191 (2010).
46. Xu, W., Jericho, M., Meinertzhagen, I. & Kreuzer, H. Digital in-line holography for biological applications. *Proc. Natl Acad. Sci. USA* **98**, 11301–11305 (2001).
47. Guo, C. et al. Quantitative multi-height phase retrieval via a coded image sensor. *Biomed. Opt. Express* **12**, 7173–7184 (2021).
48. Abels, E. & Pantanowitz, L. Current state of the regulatory trajectory for whole slide imaging devices in the USA. *J. Pathol. Inform.* **8**, 23 (2017).
49. Bian, Z. et al. Autofocusing technologies for whole slide imaging and automated microscopy. *J. Biophotonics* **13**, e202000227 (2020).
50. Wang, T. et al. Remote referencing strategy for high-resolution coded ptychographic imaging. *Opt. Lett.* **48**, 485–488 (2023).
51. Chan, A. C. et al. Parallel Fourier ptychographic microscopy for high-throughput screening with 96 cameras (96 eyes). *Sci. Rep.* **9**, 1–12 (2019).
52. Wakefield, D. L. et al. Cellular analysis using label-free parallel array microscopy with Fourier ptychography. *Biomed. Opt. Express* **13**, 1312–1327 (2022).
53. Li, P. & Maiden, A. Lensless LED matrix ptychographic microscope: problems and solutions. *Appl. Opt.* **57**, 1800–1806 (2018).
54. Shu, Y. et al. Adaptive optical quantitative phase imaging based on annular illumination Fourier ptychographic microscopy. *PhotoniX* **3**, 1–15 (2022).
55. Horstmeyer, R., Ou, X., Zheng, G., Willems, P. & Yang, C. Digital pathology with Fourier ptychography. *Comput. Med. Imaging Graph.* **42**, 38–43 (2015).
56. Williams, A. J. et al. Fourier ptychographic microscopy for filtration-based circulating tumor cell enumeration and analysis. *J. Biomed. Opt.* **19**, 066007 (2014).
57. Chen, J. et al. Rapid full-color Fourier ptychographic microscopy via spatially filtered color transfer. *Photonics Res.* **10**, 2410–2421 (2022).
58. Ou, X., Horstmeyer, R., Yang, C. & Zheng, G. Quantitative phase imaging via Fourier ptychographic microscopy. *Opt. Lett.* **38**, 4845–4848 (2013).
59. Jiang, S. et al. Wide-field, high-resolution lensless on-chip microscopy via near-field blind ptychographic modulation. *Lab Chip* **20**, 1058–1065 (2020).
60. Sun, J., Zuo, C., Zhang, J., Fan, Y. & Chen, Q. High-speed Fourier ptychographic microscopy based on programmable annular illuminations. *Sci. Rep.* **8**, 1–12 (2018).
61. Tian, L. et al. Computational illumination for high-speed in vitro Fourier ptychographic microscopy. *Optica* **2**, 904–911 (2015).
62. Chowdhury, S. et al. High-resolution 3D refractive index microscopy of multiple-scattering samples from intensity images. *Optica* **6**, 1211–1219 (2019).
63. Guo, C. et al. Depth-multiplexed ptychographic microscopy for high-throughput imaging of stacked bio-specimens on a chip. *Biosens. Bioelectron.* **224**, 115049 (2023).
64. Chung, J., Ou, X., Kulkarni, R. P. & Yang, C. Counting white blood cells from a blood smear using Fourier ptychographic microscopy. *PloS ONE* **10**, e0133489 (2015).
65. Song, P. et al. Optofluidic ptychography on a chip. *Lab Chip* **21**, 4549–4556 (2021).
66. Maiden, A. M., Humphry, M. J. & Rodenburg, J. Ptychographic transmission microscopy in three dimensions using a multi-slice approach. *J. Opt. Soc. Am. A* **29**, 1606–1614 (2012).
67. Dong, S., Nanda, P., Shiradkar, R., Guo, K. & Zheng, G. High-resolution fluorescence imaging via pattern-illuminated Fourier ptychography. *Opt. Express* **22**, 20856–20870 (2014).
68. Guo, K. et al. 13-fold resolution gain through turbid layer via translated unknown speckle illumination. *Biomed. Opt. Express* **9**, 260–275 (2018).
69. Yeh, L.-H., Chowdhury, S. & Waller, L. Computational structured illumination for high-content fluorescence and phase microscopy. *Biomed. Opt. Express* **10**, 1978–1998 (2019).
70. Dong, S., Nanda, P., Guo, K., Liao, J. & Zheng, G. Incoherent Fourier ptychographic photography using structured light. *Photonics Res.* **3**, 19–23 (2015).
71. Ou, X., Horstmeyer, R., Zheng, G. & Yang, C. High numerical aperture Fourier ptychography: principle, implementation and characterization. *Opt. Express* **23**, 3472–3491 (2015).
72. Sun, J., Zuo, C., Zhang, L. & Chen, Q. Resolution-enhanced Fourier ptychographic microscopy based on high-numerical-aperture illuminations. *Sci. Rep.* **7**, 1–11 (2017).
73. Zheng, G. *Fourier Ptychographic Imaging: A Matlab Tutorial* (Morgan & Claypool Publishers, 2016).

74. Phillips, Z. F., Eckert, R. & Waller, L. Quasi-dome: a self-calibrated high-NA LED illuminator for Fourier ptychography. In *Imaging Systems and Applications* (Optica Publishing Group, 2017).
75. Pan, A. et al. Subwavelength resolution Fourier ptychography with hemispherical digital condensers. *Opt. Express* **26**, 23119–23131 (2018).
76. Guo, K., Dong, S., Nanda, P. & Zheng, G. Optimization of sampling pattern and the design of Fourier ptychographic illuminator. *Opt. Express* **23**, 6171–6180 (2015).
77. Yeh, L.-H. et al. Experimental robustness of Fourier ptychography phase retrieval algorithms. *Opt. Express* **23**, 33214–33240 (2015).
78. Maiden, A., Johnson, D. & Li, P. Further improvements to the ptychographical iterative engine. *Optica* **4**, 736–745 (2017).
79. Bian, Z., Dong, S. & Zheng, G. Adaptive system correction for robust Fourier ptychographic imaging. *Opt. Express* **21**, 32400–32410 (2013).
80. Yang, L., Liu, Z., Zheng, G. & Chang, H. Batch-based alternating direction methods of multipliers for Fourier ptychography. *Opt. Express* **30**, 34750–34764 (2022).
81. Dong, S., Shiradkar, R., Nanda, P. & Zheng, G. Spectral multiplexing and coherent-state decomposition in Fourier ptychographic imaging. *Biomed. Opt. Express* **5**, 1757–1767 (2014).
82. Song, P. et al. Synthetic aperture ptychography: coded sensor translation for joint spatial-Fourier bandwidth expansion. *Photonics Res.* **10**, 1624–1632 (2022).
83. Guizar-Sicairos, M., Thurman, S. T. & Fienup, J. R. Efficient subpixel image registration algorithms. *Opt. Lett.* **33**, 156–158 (2008).
84. Bian, L. et al. Content adaptive illumination for Fourier ptychography. *Opt. Lett.* **39**, 6648–6651 (2014).
85. Tian, L., Li, X., Ramchandran, K. & Waller, L. Multiplexed coded illumination for Fourier Ptychography with an LED array microscope. *Biomed. Opt. Express* **5**, 2376–2389 (2014).
86. Fan, Y. et al. Efficient synthetic aperture for phaseless Fourier ptychographic microscopy with hybrid coherent and incoherent illumination. *Laser Photonics Rev.* **17**, 2200201 (2023).
87. Dong, S., Bian, Z., Shiradkar, R. & Zheng, G. Sparsely sampled Fourier ptychography. *Opt. Express* **22**, 5455–5464 (2014).
88. Song, P. et al. Freeform illuminator for computational microscopy. *Intell. Comput.* **2**, 0015 (2023).

Acknowledgements

We thank Z. Bian and A. Pirhanov for their assistance in sample preparation. This work was partially supported by the UConn SPARK grant, UConn Research Excellence Program, National Science Foundation award 2012140 and National Institute of Health award U01-NS113873. P.S. also acknowledges the support of the Thermo Fisher Scientific Fellowship.

Author contributions

G.Z. conceived the project. S.J., P.S. and G.Z. designed the pipeline. S.J., P.S., T.W. and G.Z. developed the prototype systems and prepared the display items. S.J., P.S., T.W. and L.Y. developed the data acquisition and processing pipelines for the protocol. T.W. and C.G. prepared all SolidWorks design files for the protocols. All authors contributed to the writing of the manuscript.

Competing interests

G.Z. is a named inventor on the following patents related to Fourier ptychography (US Patent, nos. 9,817,224, 9,864,184, 9,497,379) and coded ptychography (US Patent, no. 11,487,099).

Additional information

Supplementary information The online version contains supplementary material available at https://doi.org/10.1038/s41596-023-00829-4.

Correspondence and requests for materials should be addressed to Guoan Zheng.

Peer review information *Nature Protocols* thanks Zhengjun Liu, Fucai Zhang and the other, anonymous, reviewer(s) for their contribution to the peer review of this work.

Reprints and permissions information is available at www.nature.com/reprints.

Received: 6 September 2022; Accepted: 3 March 2023;
Published online: 29 May 2023

Related links

Key references using this protocol

Zheng, G. et al. *Nat. Photonics* **7**, 739-745 (2013): https://doi.org/10.1038/nphoton.2013.187
Jiang, S. et al. *ACS Photonics* **8**, 3261-3271 (2021): https://doi.org/10.1021/acsphotonics.1c01085
Jiang, S. et al. *Biosens. Bioelectron.* **196**, 113699 (2022): https://doi.org/10.1016/j.bios.2021.113699

nature portfolio

Corresponding author(s): Guoan Zheng

Last updated by author(s): 2023-02-12

Reporting Summary

Nature Portfolio wishes to improve the reproducibility of the work that we publish. This form provides structure for consistency and transparency in reporting. For further information on Nature Portfolio policies, see our Editorial Policies and the Editorial Policy Checklist.

Please do not complete any field with "not applicable" or n/a. Refer to the help text for what text to use if an item is not relevant to your study.
For final submission: please carefully check your responses for accuracy; you will not be able to make changes later.

Statistics

For all statistical analyses, confirm that the following items are present in the figure legend, table legend, main text, or Methods section.

n/a Confirmed

● ○ The exact sample size (n) for each experimental group/condition, given as a discrete number and unit of measurement

● ○ A statement on whether measurements were taken from distinct samples or whether the same sample was measured repeatedly

● ○ The statistical test(s) used AND whether they are one- or two-sided
Only common tests should be described solely by name; describe more complex techniques in the Methods section.

● ○ A description of all covariates tested

● ○ A description of any assumptions or corrections, such as tests of normality and adjustment for multiple comparisons

●

○ A full description of the statistical parameters including central tendency (e.g. means) or other basic estimates (e.g. regression coefficient) AND variation (e.g. standard deviation) or associated estimates of uncertainty (e.g. confidence intervals)

● ○ For null hypothesis testing, the test statistic (e.g. F, t, r) with confidence intervals, effect sizes, degrees of freedom and P value noted
Give P values as exact values whenever suitable.

● ○ For Bayesian analysis, information on the choice of priors and Markov chain Monte Carlo settings

● ○ For hierarchical and complex designs, identification of the appropriate level for tests and full reporting of outcomes

● ○ Estimates of effect sizes (e.g. Cohen's d, Pearson's r), indicating how they were calculated

Our web collection on statistics for biologists contains articles on many of the points above.

Software and code

Policy information about availability of computer code

Data collection	Custom acquisition codes for FP and CP (Supplementary Software) were used for data collection with MATLAB (MathWorks, MATLAB 2022).
Data analysis	Custom recovery codes for FP and CP (Supplementary Software) were used for data analysis with MATLAB (MathWorks, MATLAB 2022).

For manuscripts utilizing custom algorithms or software that are central to the research but not yet described in published literature, software must be made available to editors and reviewers. We strongly encourage code deposition in a community repository (e.g. GitHub). See the Nature Portfolio guidelines for submitting code & software for further information.

Data

Policy information about availability of data

All manuscripts must include a data availability statement. This statement should provide the following information, where applicable:
- Accession codes, unique identifiers, or web links for publicly available datasets
- A description of any restrictions on data availability
- For clinical datasets or third party data, please ensure that the statement adheres to our policy

The data supporting this study are available within the article, Supplementary Data, and the primary supporting study (Ref. 10,11,14). Experimental datasets for both setups in this study are available in Zenodo: https://doi.org/10.5281/zenodo.7492626.

Human research participants

Policy information about studies involving human research participants and Sex and Gender in Research.

Reporting on sex and gender	N/A
Population characteristics	N/A
Recruitment	N/A
Ethics oversight	N/A

Note that full information on the approval of the study protocol must also be provided in the manuscript.

Field-specific reporting

Please select the one below that is the best fit for your research. If you are not sure, read the appropriate sections before making your selection.

● Life sciences ○ Behavioural & social sciences ○ Ecological, evolutionary & environmental sciences

Life sciences study design

All studies must disclose on these points even when the disclosure is negative.

Sample size	The biological samples used in this study were solely to support the demonstration of imaging performance of our platform.
Data exclusions	No data were excluded for the analysis
Replication	N/A, no such experimental groups in this study
Randomization	N/A, no such experimental groups in this study
Blinding	N/A, no such experimental groups in this study

Behavioural & social sciences study design

All studies must disclose on these points even when the disclosure is negative.

Study description	
Research sample	
Sampling strategy	
Data collection	
Timing	
Data exclusions	
Non-participation	
Randomization	

Ecological, evolutionary & environmental sciences study design

All studies must disclose on these points even when the disclosure is negative.

Study description	
Research sample	
Sampling strategy	
Data collection	
Timing and spatial scale	
Data exclusions	
Reproducibility	
Randomization	

Blinding

Did the study involve field work? ○ Yes ○ No

Field work, collection and transport

Field conditions

Location

Access & import/export

Disturbance

Reporting for specific materials, systems and methods

We require information from authors about some types of materials, experimental systems and methods used in many studies. Here, indicate whether each material, system or method listed is relevant to your study. If you are not sure if a list item applies to your research, read the appropriate section before selecting a response.

Materials & experimental systems

n/a	Involved in the study
○	○ Antibodies
○	○ Eukaryotic cell lines
○	○ Palaeontology and archaeology
○	○ Animals and other organisms
○	○ Clinical data
○	○ Dual use research of concern

Methods

n/a	Involved in the study
○	○ ChIP-seq
○	○ Flow cytometry
○	○ MRI-based neuroimaging

Antibodies

Antibodies used

Validation

Eukaryotic cell lines

Policy information about cell lines and Sex and Gender in Research

Cell line source(s)

Authentication

Mycoplasma contamination

Commonly misidentified lines
(See ICLAC register)

Palaeontology and Archaeology

Specimen provenance

Specimen deposition

Dating methods

☐ Tick this box to confirm that the raw and calibrated dates are available in the paper or in Supplementary Information.

Ethics oversight

Note that full information on the approval of the study protocol must also be provided in the manuscript.

Animals and other research organisms

Policy information about studies involving animals; ARRIVE guidelines recommended for reporting animal research, and Sex and Gender in Research

Laboratory animals: Goat blood

Wild animals: Not involved in this study

Reporting on sex: Not involved in this study

Field-collected samples: Not involved in this study

Ethics oversight: Animal protocol procedures were reviewed and approved by the Institutional Animal Care and Use Committee of University of

Note that full information on the approval of the study protocol must also be provided in the manuscript.

Clinical data

Policy information about clinical studies

All manuscripts should comply with the ICMJE guidelines for publication of clinical research and a completed CONSORT checklist must be included with all submissions.

Clinical trial registration:

Study protocol:

Data collection:

Outcomes:

Dual use research of concern

Policy information about dual use research of concern

Hazards

Could the accidental, deliberate or reckless misuse of agents or technologies generated in the work, or the application of information presented in the manuscript, pose a threat to:

No | Yes
- ○ ○ Public health
- ○ ○ National security
- ○ ○ Crops and/or livestock
- ○ ○ Ecosystems
- ○ ○ Any other significant area

Experiments of concern

Does the work involve any of these experiments of concern:

No | Yes
- ○ ○ Demonstrate how to render a vaccine ineffective
- ○ ○ Confer resistance to therapeutically useful antibiotics or antiviral agents
- ○ ○ Enhance the virulence of a pathogen or render a nonpathogen virulent
- ○ ○ Increase transmissibility of a pathogen
- ○ ○ Alter the host range of a pathogen
- ○ ○ Enable evasion of diagnostic/detection modalities
- ○ ○ Enable the weaponization of a biological agent or toxin
- ○ ○ Any other potentially harmful combination of experiments and agents

ChIP-seq

Data deposition

☐ Confirm that both raw and final processed data have been deposited in a public database such as GEO.

☐ Confirm that you have deposited or provided access to graph files (e.g. BED files) for the called peaks.

Data access links
May remain private before publication.

Files in database submission

Genome browser session
(e.g. UCSC)

Methodology

Replicates

Sequencing depth

Antibodies

Peak calling parameters

Data quality

Software

Flow Cytometry

Plots

Confirm that:

☐ The axis labels state the marker and fluorochrome used (e.g. CD4-FITC).

☐ The axis scales are clearly visible. Include numbers along axes only for bottom left plot of group (a 'group' is an analysis of identical markers).

☐ All plots are contour plots with outliers or pseudocolor plots.

☐ A numerical value for number of cells or percentage (with statistics) is provided.

Methodology

Sample preparation

Instrument

Software

Cell population abundance

Gating strategy

☐ Tick this box to confirm that a figure exemplifying the gating strategy is provided in the Supplementary Information.

Magnetic resonance imaging

Experimental design

Design type

Design specifications

Behavioral performance measures

Acquisition

Imaging type(s)

Field strength

Sequence & imaging parameters

Area of acquisition

Diffusion MRI ○ Used ○ Not used

Preprocessing

Preprocessing software

Normalization

Normalization template

Noise and artifact removal

Volume censoring

Statistical modeling & inference

Model type and settings

Effect(s) tested

Specify type of analysis: ○ Whole brain ○ ROI-based ○ Both

Statistic type for inference
(See Eklund et al. 2016)

Correction

Models & analysis

n/a	Involved in the study
○	○ Functional and/or effective connectivity
○	○ Graph analysis
○	○ Multivariate modeling or predictive analysis

Functional and/or effective connectivity

Graph analysis

Multivariate modeling and predictive analysis